

The Implicit Bias of Logit Regularization

Alon Beck¹ Yohai Bar-Sinai^{1,2,3} Noam Levi⁴

Abstract

Logit regularization, the addition a convex penalty directly in logit space, is widely used in modern classifiers, with label smoothing as a prominent example. While such methods often improve calibration and generalization, their mechanism remains under-explored. In this work, we analyze a general class of such logit regularizers in the context of linear classification, and demonstrate that they induce an implicit bias of *logit clustering* around finite per-sample targets. For Gaussian data, or whenever logits are sufficiently clustered, we prove that logit clustering drives the weight vector to align exactly with *Fisher’s Linear Discriminant*. To demonstrate the consequences, we study a simple signal-plus-noise model in which this transition has dramatic effects: Logit regularization halves the critical sample complexity and induces grokking in the small-noise limit, while making generalization robust to noise. Our results extend the theoretical understanding of label smoothing and highlight the efficacy of a broader class of logit-regularization methods.

1. Introduction

Modern deep learning models are frequently trained with Label Smoothing (LS) (Szegedy et al., 2016) or similar regularization techniques to improve generalization and calibration (Müller et al., 2019). The empirical benefits of these methods are well-documented, and their success is often attributed to the prevention of overconfidence. However, a theoretical understanding of their underlying mechanics remains incomplete.

In this work, we investigate the geometric mechanism of a

¹Raymond and Beverly Sackler School of Physics and Astronomy, Tel-Aviv University, Tel-Aviv 69978, Israel ²Racah Institute of Physics, The Hebrew University of Jerusalem, Edmond J. Safra Campus, Jerusalem 9190401, Israel ³The Rachel and Selim Benin School of Computer Science and Engineering, The Hebrew University of Jerusalem, Edmond J. Safra Campus, Jerusalem 9190401, Israel ⁴École Polytechnique Fédérale de Lausanne (EPFL), Switzerland. Correspondence to: Alon Beck <alonbk2@gmail.com>.

broader class of regularizers: *convex logit regularization*, of which Label Smoothing is one instance. Our central observation is that LS causes clustering of logits.

Unlike weight-based regularization schemes, such as L_2 , or ridge regularization (Tikhonov and Arsenin, 1977), LR allows a per-sample decomposition of the loss as $\mathcal{L} = N^{-1} \sum_i \ell(z_i, y_i)$, where z_i and y_i denote the logit and class of the i -th sample, respectively, and N is the number of samples. A convex logit penalty generically creates a finite global minimum for ℓ , and thus gradient descent performs *logit clustering* around these finite targets in logit space. This is in contrast to unregularized logistic regression, in which gradient descent is equivalent to margin maximization (Soudry et al., 2018; Ji and Telgarsky, 2019; Lyu and Li, 2020). Leveraging this insight, we derive several surprising consequences of logit-regularization. We summarize our main contributions below:

- **The implicit bias of Logit regularization:** We demonstrate that logit regularization fundamentally shifts the optimization objective from margin maximization to logit clustering around finite per-sample targets. For Gaussian data or quadratic per-sample loss, we prove that this clustering objective drives the weight vector S to align exactly with *Fisher’s Linear Discriminant* (Fisher, 1936), $S \propto \Sigma^{-1} \mu$.
- **Insensitivity to the regularizer:** Beyond the solvable Gaussian/quadratic cases, we argue the same direction holds approximately whenever the data is near-Gaussian or when logits concentrate near their targets (making the loss locally quadratic). As this direction depends only on data geometry, generalization accuracy becomes largely insensitive to the regularizer’s functional form and strength.
- We assume a signal-plus-noise decomposition of the data, that splits the noisy part of the input features into a signal-aligned component and an orthogonal complement. In this setting, we demonstrate the following.
 - **Shift in the Interpolation Threshold and grokking:** In the limit of noiseless features (where the noise component along the signal direction is zero) and working in the high-dimensional proportional regime of $d, N \rightarrow \infty$ (where d is the

input dimension), logit regularization shifts the interpolation threshold from the standard separability limit $\lambda_c = d/N = 1/2$ (Cover, 1965; Gardner, 1988; Beck et al., 2025) to $\lambda_c = 1$. Notably, under weak regularization, we identify *grokking* dynamics (delayed generalization accompanied by non-monotonic test loss dynamics) in the region $1/2 < \lambda < 1$.

- **Invariance to Orthogonal Noise:** We prove that the optimal generalization accuracy is invariant to the amplitude of orthogonal noise. This observation allows us to construct a *phase diagram* delineating the specific regimes (defined by signal noise and orthogonal noise amplitudes) where logit regularization yields a generalization benefit over the unregularized baseline.

We validate our theoretical predictions numerically on Gaussian data and on a more realistic distribution using ResNet-18 (He et al., 2015) embeddings from the CIFAR-10 dataset (Krizhevsky, 2009).

2. Related Work

Here, we provide a focused review of the prior research most central to our contribution. For an additional detailed literature survey, including variants of LS and technical high-dimensional solvers, we refer the reader to App. A.

Logit Regularization. Label smoothing (LS) (Szegedy et al., 2016) is a standard tool for improving generalization and calibration (Müller et al., 2019; Guo et al., 2017). It is a specific instance of a broader class of logit-space penalties, including entropy-based (Pereyra et al., 2017) and logit-norm (Dauphin and Cubuk, 2021) regularizers. While these are often motivated by the prevention of overconfidence, our work provides a geometric characterization of how these penalties replace unbounded margin growth with a *logit clustering* objective.

Implicit Bias and High-Dimensional Asymptotics. For unregularized classification, the implicit bias of gradient descent leads to the hard-margin SVM/max-margin separator (Soudry et al., 2018; Lyu and Li, 2020). We contrast this with the finite per-sample optima created by logit regularization. Our analysis connects to high-dimensional theories of linear separability (Cover, 1965; Gardner, 1988) and recent asymptotics for overparameterized classifiers (Montanari et al., 2019; Mignacco et al., 2020; Wang and Thrampoulidis, 2022).

Grokking and Neural Collapse. Grokking, a delayed transition to generalization, was originally observed in algorithmic tasks (Power et al., 2022). The most relevant works in this field relate the edge of separability in logistic regression

with grokking transitions (Beck et al., 2025). In multi-class settings, are results are reminiscent of *neural collapse* (Papyan et al., 2020), a phenomenon in which logits arrange in simplex configurations (Zhou et al., 2022; Garrod and Keating, 2025).

3. The Implicit Bias of Logit Regularization

3.1. Setup: Logit Regularization as a Generalization of Label Smoothing

We study linear classifiers. For conceptual clarity, we focus initially on the binary setting with zero bias ($b = 0$). In this case, the model outputs a scalar logit $z_i = \mathbf{S}^\top \mathbf{x}_i$ where \mathbf{x}_i are the data points, and \mathbf{S} is model weights vector. The extension to the multi-class setting is provided in Sec. 7.

We consider a class of loss functions $\mathcal{L} = N^{-1} \sum_{i=1}^N \ell(z_i, y_i)$, where z_i is the logit and $y_i \in \{-1, +1\}$ is label of the i -th sample, respectively. We consider the per-sample loss

$$\ell(z, y) = (1 - \alpha)\ell_{\text{CE}}(z, y) + \alpha f(z), \quad (1)$$

where $\ell_{\text{CE}}(z, y) = \log(1 + e^{-yz})$ is the standard cross-entropy loss, $f(z)$ is a convex and even *logit regularization* function, and $\alpha \in [0, 1]$ controls the regularization amplitude. Notably, standard Label Smoothing (LS) is a specific instance of this framework, corresponding to the choice $f(z) = \log(2 + 2 \cosh z)$ (See App. B). While most of our results do not depend on the exact form f , for simplicity, we will consider $f(z) = z^2$ in all our numerical results.

Since ℓ_{CE} depends only on the product yz and f is even, the loss depends strictly on the signed logit. For notational simplicity, from here on we redefine $z \leftarrow yz$. Equivalently, we absorb the label into the input vector, $\mathbf{x} \leftarrow y\mathbf{x}$, such that the logit remains $z_i = \mathbf{S}^\top \mathbf{x}_i$. This allows us to analyze the univariate function $\ell(z)$ independently of the class label.

Distinction from L_2 regularization: We emphasize that this formulation differs significantly from standard parameter regularization. While logit regularization acts on the model logits independently, L_2 penalty implicitly couples data samples via the global norm. This prevents decomposing the loss into independent per-sample terms, a property central to all of our analysis throughout this work.

3.2. Logit Clustering

The introduction of logit regularization fundamentally alters the optimization landscape. In the unregularized case ($\alpha = 0$), the per-sample cross-entropy loss ℓ_{CE} is monotonic, and the optimal solution maximizes the margins (Soudry et al., 2018; Ji and Telgarsky, 2019). When the data is linearly separable, this implicit bias drives the weight norm $\|\mathbf{S}\| \rightarrow \infty$, potentially leads to overconfidence and

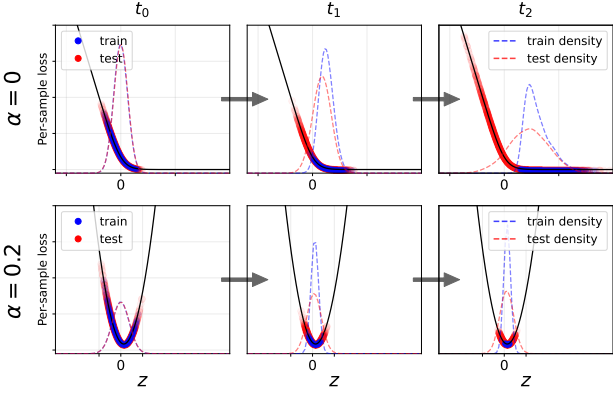


Figure 1. Logit regularization induces clustering. Logit evolution for a linear classifier trained on Gaussian data (see App. E.6 for more details regarding the setup). The train (blue) and test (red) samples are visualized across three training epochs (early, middle, and final). Note that samples are classified correctly if $z > 0$. **Top** ($\alpha = 0$): The unregularized logits are pushed toward infinity to maximize margins, indicating overconfidence. **Bottom** ($\alpha > 0$): The regularized loss exhibits a distinct finite minimum, driving the logits to cluster tightly around a target value z^* during training. Note the looser clustering on the test set due to the misalignment between the empirical noise direction and the true signal.

overfitting (see Figure 1, top row). In contrast, when $\alpha > 0$, the per-sample loss $\ell(z)$ has a unique finite global minimum denoted by z^* . Clearly, the loss has a data-independent lower bound, $\mathcal{L} \geq z^*$, which is achieved only if $z_i = z^*$ for all samples. However, given the linear constraint $z_i = \mathbf{S}^\top \mathbf{x}_i$, the model generally cannot collapse all samples to a single point. Consequently, the optimization process becomes a geometric compromise: the model seeks a weight vector \mathbf{S} that **clusters all logits as tightly as possible around the target z^*** . This phenomenon is visualized in the bottom row of Figure 1. While logit clustering is a known effect of label smoothing (Müller et al., 2019), we will show that this straightforward observation has important consequences.

3.3. Alignment with Fisher’s Linear Discriminant

In this section, we derive the exact form of the implicit bias of logit regularization for logistic regression under idealized conditions, and show that logit clustering in this case drives the weight vector to be in the direction of Fisher’s Linear Discriminant. Specifically, we consider two regimes: (i) Gaussian data with any convex regularizer, and (ii) arbitrary data distributions with a quadratic per-sample loss¹. In both cases, we first demonstrate that the optimization problem is equivalent to minimizing the *coefficient of variation* (CV) $r(\mathbf{S}) \equiv \sigma(\mathbf{S})/\mu(\mathbf{S})$, where $\mu(\mathbf{S}), \sigma(\mathbf{S})$ are the logits mean and standard deviation, as a function of the weights.

¹ Almost any per-sample loss as defined in Eq. (1) can be considered quadratic close enough to its minimum.

Proposition 3.1 (Gaussian Data). *Let $\mathbf{x} \sim \mathcal{N}(\mu_x, \Sigma_x)$ with $\mu_x \neq \mathbf{0} \in \mathbb{R}^d$, and consider a vector $\mathbf{S} \in \mathbb{R}^d$. The logit $z(\mathbf{S}) = \mathbf{S}^\top \mathbf{x}$ is Gaussian with mean $\mu(\mathbf{S}) = \mathbf{S}^\top \mu_x$ and variance $\sigma^2(\mathbf{S}) = \mathbf{S}^\top \Sigma_x \mathbf{S}$. Define $L(\mathbf{S}) = \mathbb{E}[\ell(z(\mathbf{S}))]$, where $\ell(z)$ is a convex function with a unique minimum.*

Then, the optimum $\mathbf{S}_{\min} = \arg \min_{\mathbf{S}} L(\mathbf{S})$ minimizes the ratio $r(\mathbf{S}) = \sigma(\mathbf{S})/\mu(\mathbf{S})$. That is, $r(\mathbf{S}_{\min}) \leq r(\mathbf{S}) \forall \mathbf{S} \in \mathbb{R}^d$.

Proof. Let $Q : \mathbb{R}^d \rightarrow \mathbb{R}^2$ be mapping from weights to logit moments, $Q(\mathbf{S}) = (\mu(\mathbf{S}), \sigma(\mathbf{S}))$. Since z is normally distributed, L is completely determined by its moments $\mu(\mathbf{S})$ and $\sigma(\mathbf{S})$ and optimization in weight space is equivalent to a constrained optimization problem in moment space. Let $\Omega \subset \mathbb{R}^2$ be the set of attainable moments, ie the image of \mathbb{R}^d under Q .

Since both $\mu(\mathbf{S})$ and $\sigma(\mathbf{S})$ scale linearly in \mathbf{S} (e.g., $\mu(\lambda \mathbf{S}) = \lambda \mu(\mathbf{S})$), each ray in weight space is mapped to a ray in Ω . Therefore, Ω is a cone composed of rays emanating from the origin:

$$\Omega = \{(\mu, r\mu) \mid \mu > 0, r_1 \leq r \leq r_2\}, \quad (2)$$

where we assumed without loss of generality that $\mu > 0$ and r_2 may be infinite.

Using standard convexity arguments, it is easy to show that for any fixed mean μ , L is an increasing function of the spread σ (see Lemma C.1 in the Appendix). Therefore, optimum in Ω is attained on its lower boundary, namely the ray with the minimal slope r_1 . Thus, \mathbf{S}_{\min} in mapped under Q to the minimal $r = \sigma/\mu$. \square

Corollary 3.2 (Quadratic Loss for any data). *For any data distribution, if the per-sample loss is quadratic, i.e., $\ell(z) = a(z - z^*)^2$, then the optimal direction $\hat{\mathbf{S}}_{\min}$ minimizes the ratio $r = \sigma/\mu$.*

Proof. If ℓ is quadratic function then the loss is completely determined by the first and second moments of z .

$$L(\mathbf{S}) = \mathbb{E}[\ell(z(\mathbf{S}))] = a\sigma^2(\mathbf{S}) + (\mu(\mathbf{S}) - z^*)^2$$

Therefore, the argument of Proposition 3.1 applies verbatim. \square

We now state the main result: under these conditions, the implicit bias of logit regularization aligns the weights with Fisher’s Linear Discriminant solution.

Corollary 3.3 (LDA direction). *If the data is Gaussian, the optimal weight direction is $\hat{\mathbf{S}}_{\min} \propto \Sigma^{-1} \mu$. Similarly, if $\lambda = d/N < 1$ and the per-sample loss is quadratic, $\hat{\mathbf{S}}_{\min} \propto \Sigma^{-1} \mu$ (where Σ, μ are the empirical mean and centered covariance).*

Proof. Identifying $r(\mathbf{S})^{-1}$ as the square root of the Fisher Criterion (i.e., $(\mathbf{S}^\top \mu)^2 / \mathbf{S}^\top \Sigma \mathbf{S}$), the result follows immediately from standard LDA theory. See App. C.1 for a direct proof. \square

Outside these idealized setting, we find empirically that direction of the solution remains close to this theoretical minimum, as we will show in the next section below.

3.4. Consequence: Insensitivity to the Logit Penalty

We now turn to analyze the practical consequences this result. Even though the direction of the solution would align with LDA only when the data is purely Gaussian or the per-sample loss is completely quadratic, in practice, we expect this to hold approximately (i.e., the deviation from this direction would not be large) for a much broader set of cases: As discussed in Sec. 3.2, logit regularization tends to cluster the logits around the loss minimum. Therefore, locally, the optimal per-sample loss may be approximated as quadratic. This suggest, as we will also demonstrate numerically below, that the optimal generalization accuracy $\mathcal{A}_{\text{gen}}^{\min}$ will be quite insensitive to the specific per-sample loss $\ell(z)$, and in particular the logit regularization function $f(z)$.

Geometric Intuition. First, we will provide intuition from another perspective. As stated above, minimization of the loss now requires placing logits as tightly as possible around z^* , the minimum of $\ell(z)$. This implicitly decouple the optimization into two distinct tasks:

1. **Shape Optimization (Direction):** Making the cluster as tight as possible, by choosing a direction $\hat{\mathbf{S}} = \mathbf{S} / \|\mathbf{S}\|$ minimizing the CV $r = \sigma / \mu$.
2. **Location Optimization (Norm):** Scaling $\|\mathbf{S}\|$ to shift the logit mean μ to the proximity of z^* .

Approximately, the first task is determined solely by the dataset geometry and not by the per-loss function $\ell(z)$. Since generalization accuracy depends only on $\hat{\mathbf{S}}$ (and not $\|\mathbf{S}\|$) it should be invariant to the choice of regularization function (while the norm would be very sensitive to the per-sample minimum).

Empirical Evidence. We will now provide numerical evidence for this insensitivity. In Figure 2, we consider a binary classification experiment where the data is the mean vector $\pm(1, 0, 0, \dots)$ corresponding to the class label (arbitrarily aligned with the first axis), plus a random noise vector where each component is drawn independently from a Student-t distribution with degrees of freedom ν . Here, the logit-regularization function is taken to be $f(z) = z^2$. This is an illustrative example of a more general data model which will be discussed in detail in Sec. 4. The left panel

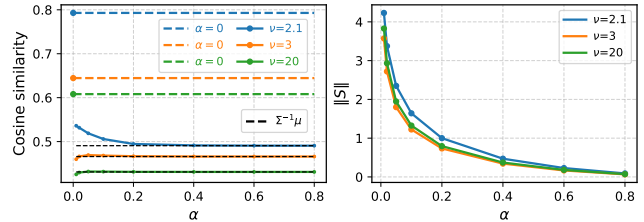


Figure 2. Change in the implicit bias and robustness to α . Analysis of the optimal weights \mathbf{S}_{\min} on Student's t-distributed data ($\nu \in \{2.1, 3, 20\}$). **Left panel:** Cosine similarity between \mathbf{S}_{\min} and the feature-axis, where the data is drawn from a Student's t-distribution for several values of ν . The dashed lines indicates the unregularized values ($\alpha = 0$). We observe an abrupt shift from $\alpha = 0$ to $\alpha > 0$, followed by a plateau that becomes flatter as ν increases (approaching a Gaussian distribution). On black dashed line we plot for comparison the limiting LDA expected value, $\Sigma^{-1}\mu$, where μ and Σ are the empirical mean and centered covariance. **Right panel:** The norm $\|\mathbf{S}_{\min}\|$, which, in contrast, exhibits a clear dependence on α . See App. E.6 for more details about the numerical setup.

shows the cosine similarity between the learned $\hat{\mathbf{S}}_{\min}$ and the true feature axis. We observe a sharp transition from the unregularized state ($\alpha = 0$) to $\alpha > 0$, indicating the *change of the implicit bias*, followed by stable plateau for $\alpha > 0$. The plateau is flatter for larger ν (approaching Gaussianity) or larger α (approaching a quadratic loss). In stark contrast, the right panel shows that the norm $\|\mathbf{S}_{\min}\|$ varies significantly with α . This confirms that logit regularization modifies the scale of the weights to satisfy the per-sample minimum, while the direction (and thus the accuracy) remains robust. For additional numerical evidence, see App. C.2.

4. Signal-plus-Noise Decomposition

Building on the geometric insight of logit clustering, we now derive several surprising consequences of logit regularization when the data distribution has a signal-plus-noise structure.

4.1. Data model

We model the data geometry via a decomposition into a signal subspace and an orthogonal noise subspace. The input $\mathbf{x} \in \mathbb{R}^d$ is generated according to

$$\mathbf{x} = y\mu_f \mathbf{e}_1 + \boldsymbol{\xi}, \quad (3)$$

where $y = \pm 1$ is the label, \mathbf{e}_1 denotes the signal direction, and μ_f represents the signal magnitude. The noise vector $\boldsymbol{\xi}$ is drawn from a zero-mean distribution with anisotropic scaling. Specifically, we define $\boldsymbol{\xi} = \sigma_f \xi_f \mathbf{e}_1 + \sigma_n \boldsymbol{\xi}_\perp$, where ξ_f and the components of $\boldsymbol{\xi}_\perp$ are drawn from distributions \mathcal{D}_f and \mathcal{D}_n (signal and noise) respectively, with zero mean. Here, σ_f and σ_n act as mixture weights. We note that in

the case of $\sigma_f = \sigma_n$ and Gaussian noise, our data generation process coincides with the noisy Gaussian mixture classification problem studied in Mignacco et al. (2020) and subsequent works.

Unless explicitly stated otherwise (e.g., in the ResNet-18 validation), we take the noise distributions to be Gaussian and align the signal with the x_1 -axis with unit amplitude (i.e., $\mu_f = 1$). Under this assumption, σ_f and σ_n represent the standard deviations of the signal-aligned and orthogonal noise components, respectively. Formally, the noise vector ξ has independent entries satisfying $\xi_1 \sim \mathcal{N}(0, \sigma_f^2)$ and $\xi_i \sim \mathcal{N}(0, \sigma_n^2)$ for all $i > 1$. The full details regarding the setup of each figure appear in Appendix E.6.

4.2. Empirical Motivation

To motivate our construction, we show that the penultimate representations of a NN trained on real-world images exhibit a geometric structure that aligns with our signal-plus-noise decomposition. Analyzing the second-order statistics, we show that the noise structure is anisotropic with respect to the task as in our suggested model.

Specifically, we consider the penultimate layer of a ResNet-18 trained on ImageNet and evaluated on CIFAR-10 (clean) versus CIFAR-10C (Hendrycks and Dietterich, 2019) (noisy). We focus on a binary task (Planes vs. Cats), and calculate for each class the empirical class means $\mu_c = \frac{1}{N_c} \sum_i \mathbf{x}_i$ and the disjoint empirical centered covariance matrices $\Sigma_c = \frac{1}{N_c} \sum_i (\mathbf{x}_i - \mu_c)(\mathbf{x}_i - \mu_c)^\top$.

To understand the noise geometry, we project these covariances matrices onto two subspaces: the signal subspace, spanned by the difference of the class means $\mathbf{v} = \mu_1 - \mu_2$, and its orthogonal complement. Computing the standard deviation along the signal axis and the root-mean-square (RMS) of the eigenvalues in the orthogonal space, we get empirical equivalents of σ_f and σ_n . As shown in Figure 3, the intra-class variance along the signal direction (σ_f) differs significantly from the variance in the orthogonal directions (σ_n). Furthermore, when the input images are corrupted (using CIFAR-10C), these noise components grow.

These observations suggests that a single isotropic noise parameter cannot fully capture the geometry of real-world representations, which justify our choice of a more expressive two-parameter model (defined by \mathcal{D}_f and \mathcal{D}_n). We will return to this exact empirical setting in Sec. 8 to validate our main theoretical predictions on real-world data.

5. The Noiseless Feature Regime

We begin by investigating logistic regression under the signal-plus-noise data decomposition, in the regime where the feature noise in the signal direction vanishes ($\sigma_f = 0$),

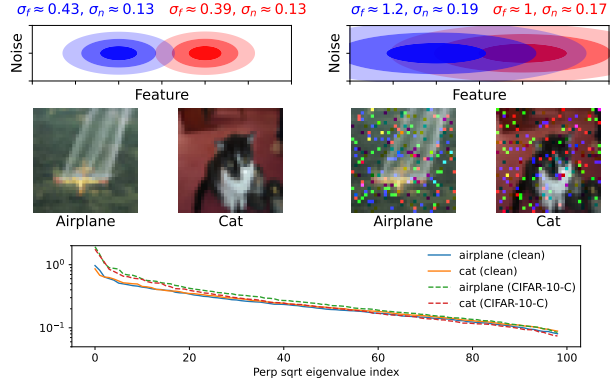


Figure 3. Effect of Input Noise on Feature Geometry. **Top Row:** Visualization of penultimate layer features for two classes (Planes vs. Cats) from ResNet-18. The horizontal axis represents the signal direction (connecting class means), while the vertical axis represents the effective orthogonal noise radius. Left: Clean CIFAR-10 data. Right: Noisy CIFAR-10C data. **Bottom Row:** The eigenspectrum of the orthogonal noise covariance matrix. For more details, see Appendix E.6.

yielding several surprising results. While idealized, the phenomena derived below persist approximately whenever the signal noise is sufficiently small ($\sigma_f \ll \mu_f, \sigma_n$).

5.1. Shift of interpolation threshold

We analyze the high-dimensional proportional limit where $d, N \rightarrow \infty$ while the ratio $\lambda = d/N$ remains fixed. In the unregularized setting, the interpolation threshold is known to occur at $\lambda_c = 1/2$ (Gardner and Derrida, 1989). The reason is tied to separability: for $\lambda > 1/2$, points in general position are linearly separable regardless of their labels. This geometric freedom allows the optimizer to satisfy the margin constraints by discovering separating directions distinct from the “true” signal $\mathbf{S} = \mathbf{e}_1$, leading to overfitting (Beck et al., 2025). In contrast, we will show that the introduction of **any** convex logit regularization will shift abruptly the interpolation threshold to $\lambda_c = 1$.

Proposition 5.1. *Let $\sigma_f = 0$ and $\alpha > 0$. Then, the minimizer of the training loss achieves perfect generalization accuracy if and only if $\lambda = d/N < 1$.*

Proof. With $\sigma_f = 0$, the signal component is deterministic: $y_i \mathbf{e}_1^\top \mathbf{x}_i = \mu_f$ for all i . Since $\alpha > 0$, the per-sample loss is strictly convex with a unique global minimum z^* .

We can construct a weight vector aligned purely with the signal, $\mathbf{S} = (z^*/\mu_f) \mathbf{e}_1$, such that $y_i \mathbf{S}^\top \mathbf{x}_i = z^*$ for all samples. This configuration achieves the global unconstrained lower bound of the total loss (the sum of per-sample minima). This solution is unique as the data matrix is full rank ($N > d$), and since it aligns perfectly with \mathbf{e}_1 , it yields 100% test accuracy.

Conversely, for $\lambda > 1$, the data matrix has a non-trivial

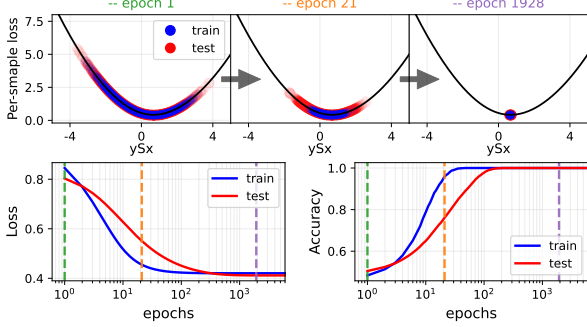


Figure 4. Perfect generalization with zero feature noise ($\sigma_f = 0$). **Top:** Evolution of the logit distribution across three training epochs. At convergence, all logits collapse to a single target value z^* . **Bottom:** Loss and accuracy over time. Vertical dashed lines indicate the epochs corresponding to the top snapshots.

null space. The loss minimizer takes the form $S_{\min} = (z^*/\mu_f)e_1 + S_{\perp}$, where $S_{\perp} \neq 0$ lies in the null space of the training data, degrading test accuracy. \square

Figure 4 demonstrates the fact that the logits collapse to a single point in this regime. Notably, this result is independent of the regularization function $f(z)$ (consistent with our previous discussion) and the orthogonal noise scale σ_n (which is not unique to $\sigma_f = 0$ as discussed below). This suggests that for sufficiently small σ_f , logit regularization is highly beneficial, effectively extending the generalization regime to $\lambda < 1$. We examine the case of non-negligible σ_f in the following section.

5.2. Grokking Dynamics.

Grokking (i.e., delayed generalization accompanied by non-monotonic test loss) has drawn significant recent attention. Developing simple analytical models that exhibit grokking is crucial for isolating the mechanisms that induce it. Previous work has identified grokking in the unregularized version of this setup, occurring near the critical threshold $\lambda_c = 1/2$ (Beck et al., 2025). Notably, we find that logit regularization can also induce grokking dynamics across the broad region $1/2 < \lambda < 1$ — see Figure 5). This occurs because the interpolation threshold is shifted to $\lambda_c = 1$. Consequently, the system exhibits delayed generalization as $\alpha \rightarrow 0$: the model initially overfits (in the direction of the unregularized implicit bias) before eventually converging to the generalizing solution. The timescale of this delay (“grokking time”) diverges as $\alpha \rightarrow 0$, consistent with previous works showing that the grokking time diverges as some control parameter is close to criticality (Levi et al., 2024).

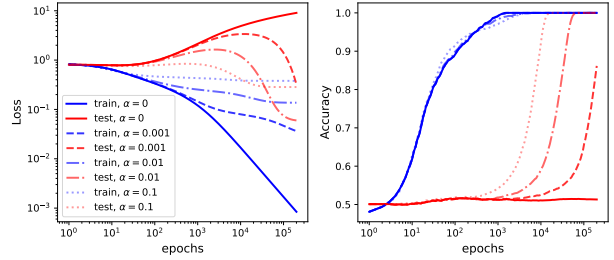


Figure 5. Grokking. Loss and accuracy curves for $\sigma_f = 0$ and $\lambda = 0.7$. While the unregularized model ($\alpha = 0$) overfits, logit regularization induces grokking (delayed generalization), with the delay diverging as α approaches zero.

6. Invariance to the Noise Scale

In this section, we show that in the presence of logit-regularization, the optimal generalization accuracy becomes independent of the orthogonal noise scale σ_n . We then use this result to map the specific regimes where logit regularization outperforms the unregularized baseline.

6.1. Proof of the Invariance

Proposition 6.1. *Let $\alpha > 0$, $\lambda = d/N < 1$, and fix σ_f, μ_f . Then, the optimal generalization accuracy $\mathcal{A}_{\text{gen}}^{\min}$ is strictly independent of σ_n .*

Proof. This follows from a simple scaling argument. Let $S_{\min} = (S_{1,\min}, S_{\perp,\min})$ denote the minimizer. The loss depends exclusively on the scalar logits $z_i = S_{1,\min}x_{i,1} + S_{\perp,\min}^T x_{i,\perp}$. Consider a rescaling of the noise variance $\sigma_n \rightarrow \beta\sigma_n$, which implies $x_{i,\perp} \rightarrow \beta x_{i,\perp}$. To maintain the optimal logit values z_{\min} (and thus minimize the loss), the weights must scale inversely: $S_{\perp,\min} \rightarrow \beta^{-1}S_{\perp,\min}$. Consequently, the product $S_{\perp,\min}^T x_{i,\perp}$ remains invariant. Since the distribution of the test logits depends on this same product, the test accuracy is invariant to σ_n . \square

Notably, while $\mathcal{A}_{\text{gen}}^{\min}$ is independent of σ_n , the direction S_{\min} is not. The cosine similarity with the feature axis e_1 , denoted by ρ , explicitly depends on the noise. Since $\|S_{\perp,\min}\| \propto \sigma_n^{-1}$, the alignment behaves as:

$$\rho_{\min} = \frac{S_{1,\min}}{\|S_{\min}\|} = \frac{1}{\sqrt{1 + (C/\sigma_n)^2}}, \quad (4)$$

where C depends on σ_f but is independent of σ_n (see Appendix E.5).

To demonstrate how can it be that the accuracy remains constant despite the changing direction of S , we examine the case of Gaussian data. The analytical expression for

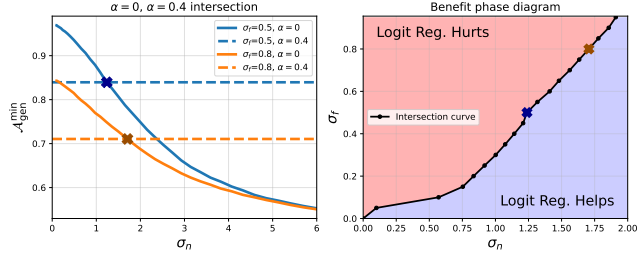


Figure 6. Benefit phase diagram. **Left:** Final generalization accuracy as a function of σ_n , comparing the unregularized ($\alpha = 0$) and regularized ($\alpha > 0$) cases, for $\lambda = 0.7$. **Right:** Phase diagram showing regions where logit regularization is beneficial. The boundary curve is constructed from the intersection points (as shown in the left panel) for different values of σ_f . For illustration, the intersection points of the unregularized and regularized curves for $\sigma_f = 0.5, 0.8$ (left) are marked as ‘X’s of corresponding colors on the boundary curve (right). For an equivalent figure in the $\lambda < 1/2$ regime, see Figure 15 in the appendix.

generalization accuracy in this case is:

$$\mathcal{A}_{\text{gen}} = \frac{1}{2} \left[1 + \text{erf} \left(\frac{\rho \mu_f}{\sqrt{2(\rho^2 \sigma_f^2 + (1 - \rho^2) \sigma_n^2)}} \right) \right]. \quad (5)$$

Substituting ρ_{\min} from Eq. (4) into Eq. (5) cancels the σ_n terms in the denominator, rendering the final accuracy explicitly independent of the noise scale. See Figure 16 in the appendix for more empirical evidence to the σ_n -invariance.

6.2. When does logit regularization help?

Since the regularized accuracy $\mathcal{A}_{\alpha>0}^{\min}$ is constant with respect to σ_n while the unregularized accuracy $\mathcal{A}_{\alpha=0}^{\min}$ change, one may find a critical noise threshold where these curves intersect. This intersection defines the point at which logit regularization becomes advantageous. For Gaussian data, we illustrate this crossover in the left panel of Figure 6. By tracing this threshold across varying σ_f , we construct the phase diagram shown in the right panel, presenting the regime where regularization improves performance.

7. Generalization to Multi-class Setting

In this section, we extend our analysis to the K -class setting, demonstrating that the core geometric mechanism of logit clustering remains the same.

7.1. Setup

We consider a linear classifier producing logits $\mathbf{z} = W\mathbf{x} + \mathbf{b}$, where $W \in \mathbb{R}^{K \times d}$. The predicted class is $c = \text{argmax}_k z_k$. Let \mathbf{y} be the one-hot label vector for class c . We minimize the empirical loss $\mathcal{L} = \frac{1}{N} \sum_i \ell(\mathbf{z}^{(i)}, \mathbf{y}^{(i)})$, where the per-

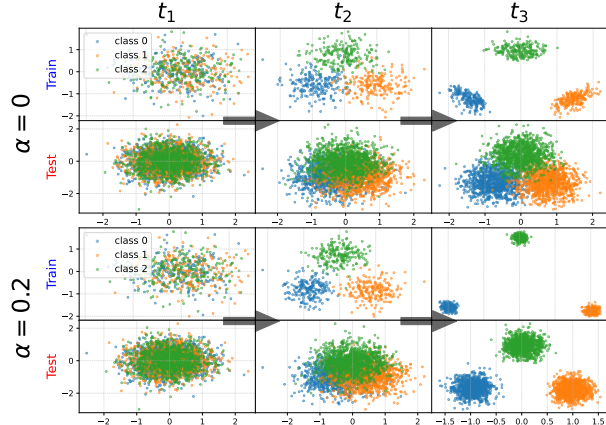


Figure 7. Multi-class Logit Clustering. Projection of the data from three classes onto the subspace spanned by the relative weight differences ($S_1 - S_2$ and $S_1 - S_3$). The parameter is set to $\lambda = d/N = 0.7$: since $\lambda > 1/2$, the data is separable. **Left ($\alpha = 0$):** Standard cross-entropy separates classes linearly, maximizing the margin. **Right ($\alpha = 0.2$):** Logit regularization enforces tight clustering around the simplex vertices.

sample loss is defined as:

$$\ell(\mathbf{z}, \mathbf{y}) = (1 - \alpha)\ell_{\text{CE}}(\mathbf{z}, \mathbf{y}) + \alpha f(\mathbf{z}). \quad (6)$$

Here, $\ell_{\text{CE}}(\mathbf{z}, \mathbf{y}) = -\sum_k y_k \log p_k$ is the standard cross-entropy loss, and $f(\mathbf{z})$ is a symmetric, convex regularization term. We note that standard LS is recovered by choosing (See Appendix B):

$$f_{\text{LS}}(\mathbf{z}) = \log \left(\sum_{k=1}^K e^{z_k} \right) - \frac{1}{K} \sum_{k=1}^K z_k. \quad (7)$$

To extend the signal-plus-noise decomposition, we assume the class means $\{\boldsymbol{\mu}_c\}_{c=1}^K$ are affinely independent, spanning a $(K-1)$ -dimensional centered signal subspace $\mathcal{S} = \text{span}\{\boldsymbol{\mu}_c - \bar{\boldsymbol{\mu}}\}_{c=1}^K$. The input \mathbf{x} for a given class c is modeled as $\mathbf{x} = \boldsymbol{\mu}_c + \boldsymbol{\xi}$. The noise vector $\boldsymbol{\xi}$ decomposes into signal-aligned and orthogonal components:

$$\boldsymbol{\xi} = \sigma_f \boldsymbol{\eta}_f + \sigma_n \boldsymbol{\eta}_n, \quad (8)$$

where $\boldsymbol{\eta}_f \in \mathcal{S}$ and $\boldsymbol{\eta}_n \in \mathcal{S}^\perp$ are drawn from standard isotropic distributions \mathcal{D}_f and \mathcal{D}_n , scaled by σ_f and σ_n , respectively.

7.2. Simplex Clustering minimization

As in the binary classification case, the introduction of regularization ($\alpha > 0$) fundamentally alters the optimization landscape. The per-sample loss now possesses a finite minimum. Explicitly writing the per-sample loss for class c (where $\mathbf{y} = \mathbf{y}_c$ is a one-hot vector with 1 at index c), we

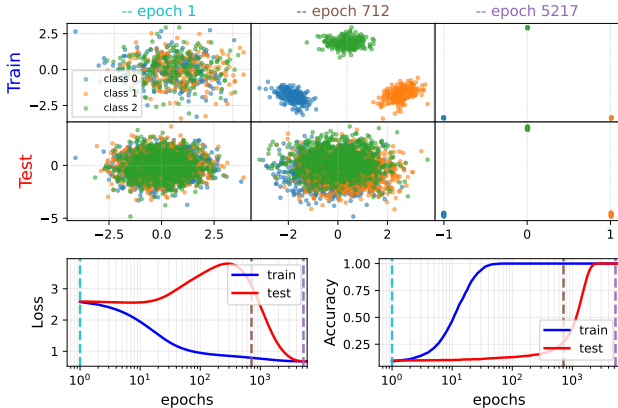


Figure 8. Grokking in Multi-class and Small Logit Regularization. Dynamics in the multi-class case, for $\sigma_f = 0$, $\lambda = 0.7$ and $\alpha = 0.04$. **Top:** Logit projections at three time-steps. The model initially learns the overfitting solution before eventually collapsing the minima of the simplex vertices, corresponding to the generalization phase. **Bottom:** Evolution of test accuracy and loss. We observe the characteristic grokking signature: the test loss initially rises (overfitting) before descending, and generalization accuracy is delayed.

obtain:

$$\ell(\mathbf{z}, \mathbf{y} = \mathbf{y}_c) = (1 - \alpha) \left(\log \left(\sum_j e^{z_j} \right) - z_c \right) + \alpha f(\mathbf{z}). \quad (9)$$

For each class c , there exists a unique target logit vector $\mathbf{z}_{(c)}^*$ that minimizes this per-sample loss. Due to permutation symmetry, this vector takes a specific form: a high value z_{high} at index c , and a uniform lower value z_{low} elsewhere. This represents the maximal certainty permitted by the regularization, corresponding to a probability distribution that peaks at class c (with a value determined by α) and uniform elsewhere.

The set of target vectors $\{\mathbf{z}_{(1)}^*, \dots, \mathbf{z}_{(K)}^*\}$ forms the vertices of a symmetric simplex in logit space. Consequently, the optimization objective transforms into a *clustering* problem: the model seeks a weight matrix W that collapses the logits of each class c as tightly as possible around its corresponding vertex $\mathbf{z}_{(c)}^*$.

This behavior is visualized in the numerical experiment presented in Figure 7. We assume Gaussian distributions for both signal and noise components. The model is trained with a quadratic regularization term $f(\mathbf{z}) = \|\mathbf{z}\|^2$. We then adopt the visualization scheme introduced in Müller et al. (2019), projecting the data of three classes onto the plane spanned by the class templates at three distinct time-steps during training. In the unregularized regime ($\alpha = 0$), the (projected) logits scatter to maximize separability. In contrast, regularization ($\alpha > 0$) forces them to cluster at the simplex vertices.

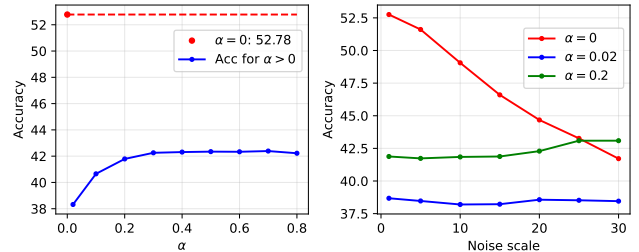


Figure 9. Validation on ResNet-18 Penultimate Features. **Left:** Generalization accuracy vs. regularization strength α . We observe a jump followed by saturation, confirming directional stability. **Right:** Accuracy vs. synthetic scaling of the orthogonal noise component. Logit regularization ($\alpha > 0$) makes the model insensitive to the noise scale, in contrast to the unregularized baseline.

Most of our key results from the binary setting extend naturally to the multi-class case: see App. D for details. For example, Figure 8 demonstrates our main finding regarding the noiseless regime: for $1/2 < \lambda < 1$ and small α , we observe grokking. First, the training samples become fully separated while the model overfits the test set. At later times, the logits switch their implicit bias due to logit-regularization, collapsing to the vertices of the simplex and obtaining perfect generalization.

8. Validation on Penultimate Layer Embeddings

The analysis above was carried out in a linear setting with an idealized signal-plus-noise decomposition. We now validate two main qualitative predictions — the sharp transition from $\alpha = 0$ to $\alpha > 0$ and the invariance to orthogonal noise scaling — in a more realistic feature space.

Setup. We use the same ResNet-18 penultimate-layer embeddings introduced in Figure 3. We freeze the representation and train only a linear classifier on top, using the loss in Eq. (6), with quadratic logit regularization $f(\mathbf{z}) = \|\mathbf{z}\|^2$. See App. E.6 for more details.

α -Insensitivity. We examine the sensitivity of the optimal generalization accuracy to the regularization strength α , see left panel of Figure 9. As predicted in Sec. 3.4, the accuracy jumps significantly and enters a stable plateau. The deviation from it at smaller α is due to the fact that the data is not a Gaussian.

σ_n -independence via synthetic orthogonal rescaling. To directly test the invariance in Proposition 6.1, we synthetically rescale only the component of each embedding that is orthogonal to the subspace spanned by the class means. This changes the effective σ_n without altering the class-mean geometry. The right panel of Figure 9 shows that the unregularized classifier ($\alpha = 0$) degrades substantially under this rescaling, whereas the regularized classifier ($\alpha > 0$)

is more robust, according to our expectations.

9. Conclusion

In this work, we have characterized the implicit bias of convex logit regularization, such as label smoothing, in linear classification. We showed that such regularization results in *logit clustering* around the finite minima of the per-sample loss function. This provides a straightforward geometric explanation for the known label-smoothing effect, and demonstrates that the phenomenon is not unique to Label Smoothing, but is a general consequence of any loss that can be decomposed as a sum of per-sample losses with a finite minimum.

Remarkably, this clustering objective is intimately connected to classical statistical discrimination. We proved that for Gaussian data or quadratic loss functions, logit regularization drives the weight vector to align exactly with *Fisher’s Linear Discriminant* ($\Sigma^{-1}\mu$). Empirically, we demonstrated that the direction remains close to this solution even beyond the idealized conditions. This result bridges a conceptual gap, showing that modern “soft target” techniques like Label Smoothing effectively recover the optimal linear discriminator for Gaussian data. These findings also suggest that the benefits of Label Smoothing are not unique to the specific functional form used in practice but are shared by a broad class of convex logit penalties.

Leveraging a signal-plus-noise decomposition, we also demonstrated that logit regularization shifts the interpolation threshold to $\lambda = 1$ (yielding perfect generalization in regimes where unregularized models fail) and induces grokking dynamics under weak regularization. Finally, we proved that regularized accuracy is invariant to orthogonal noise scaling, allowing us to map the precise phase space where regularization is beneficial.

Limitations and Future Work. Our analysis relies on a linear framework. While we validated our findings on fixed ResNet embeddings, extending the logit clustering perspective to end-to-end training (where the representation is learned jointly) remains a primary challenge. Additionally, while we characterized the implicit bias for Gaussian data as the minimization of the coefficient of variation, identifying the analogous geometric invariant for general, heavy-tailed distributions remains an open question. Future research should investigate how this “LDA-like” bias interacts with the inductive bias of deep networks during feature learning, as well as the efficacy of this broader class of convex penalties in practical deep learning settings.

References

- A. Beck, N. I. Levi, and Y. Bar-Sinai. Grokking at the edge of linear separability. In *International Conference on Machine Learning (ICML)*, 2025. URL <https://arxiv.org/abs/2410.04489>.
- M. Celentano, C. Cheng, and A. Montanari. The high-dimensional asymptotics of first order methods with random data. *arXiv preprint arXiv:2112.07572*, 2021. URL <https://arxiv.org/abs/2112.07572>.
- K. Chandrasegaran, N.-T. Tran, Y. Zhao, and N.-M. Cheung. Revisiting label smoothing and knowledge distillation compatibility: What was missing? In *Proceedings of the International Conference on Machine Learning (ICML)*, pages 2890–2916. PMLR, 2022.
- T. M. Cover. Geometrical and statistical properties of systems of linear inequalities with applications in pattern recognition. *IEEE Transactions on Electronic Computers*, EC-14(3):326–334, 1965. doi: 10.1109/PGEC.1965.264137.
- Y. Dauphin and E. D. Cubuk. Deconstructing the regularization of batchnorm. In *International Conference on Learning Representations (ICLR)*, 2021.
- Z. Deng, A. Kammoun, et al. A model of double descent for high-dimensional binary classification. *arXiv preprint arXiv:1912.00887*, 2019.
- R. A. Fisher. The use of multiple measurements in taxonomic problems. *Annals of Eugenics*, 7:179–188, 1936. doi: 10.1111/j.1469-1809.1936.tb02137.x.
- Y. Gao, W. Wang, C. Herold, Z. Yang, and H. Ney. Towards a better understanding of label smoothing in neural machine translation. In *Proceedings of the 1st Conference of the Asia-Pacific Chapter of the Association for Computational Linguistics and the 10th International Joint Conference on Natural Language Processing*, pages 212–223, 2020.
- E. Gardner. The space of interactions in neural network models. *Journal of Physics A: Mathematical and General*, 21(1):257–270, 1988.
- E. Gardner and B. Derrida. Three unfinished works on the optimal storage capacity of networks. *Journal of Physics A: Mathematical and General*, 22:1983–1994, 1989.
- C. Garrod and J. P. Keating. The persistence of neural collapse despite low-rank bias, 2025. URL <https://arxiv.org/abs/2410.23169>.
- C. Guo, G. Pleiss, Y. Sun, and K. Q. Weinberger. On calibration of modern neural networks. In *Proceedings of the International Conference on Machine Learning (ICML)*, pages 1321–1330. PMLR, 2017.

L. Guo, K. Ross, Z. Zhao, G. Andriopoulos, S. Ling, Y. Xu, and Z. Dong. Cross entropy versus label smoothing: A neural collapse perspective. *arXiv preprint arXiv:2402.03979*, 2024.

X. Y. Han, V. Petyan, and D. L. Donoho. Neural collapse under mse loss: Proximity to and dynamics on the simplex etf. In *International Conference on Learning Representations (ICLR)*, 2022. URL https://openreview.net/forum?id=w1UbdvWH_R3.

K. He, X. Zhang, S. Ren, and J. Sun. Deep residual learning for image recognition, 2015. URL <https://arxiv.org/abs/1512.03385>.

D. Hendrycks and T. Dietterich. Benchmarking neural network robustness to common corruptions and perturbations. In *International Conference on Learning Representations (ICLR)*, 2019. URL <https://arxiv.org/abs/1903.12261>.

G. Hinton, O. Vinyals, and J. Dean. Distilling the knowledge in a neural network. *arXiv preprint arXiv:1503.02531*, 2015. URL <https://arxiv.org/abs/1503.02531>.

Z. Ji and M. Telgarsky. The implicit bias of gradient descent on nonseparable data. In *Proceedings of The 32nd Conference on Learning Theory (COLT)*, 2019. URL <https://proceedings.mlr.press/v99/ji19a.html>.

S. Kornblith, T. Chen, H. Lee, and M. Norouzi. Why do better loss functions lead to less transferable features? *Advances in Neural Information Processing Systems (NeurIPS)*, 34:28648–28662, 2021.

A. Krizhevsky. Learning multiple layers of features from tiny images. Technical report, University of Toronto, 2009.

D. Lee, K. C. Cheung, and N. L. Zhang. Adaptive label smoothing with self-knowledge in natural language generation. *arXiv preprint arXiv:2210.13459*, 2022.

N. I. Levi, A. Beck, and Y. Bar-Sinai. Grokking in linear estimators – a solvable model that groks without understanding. In *International Conference on Learning Representations (ICLR)*, 2024. URL <https://openreview.net/forum?id=GH2LYb9XV0>.

J. Liang, L. Li, Z. Bing, B. Zhao, Y. Tang, B. Lin, and H. Fan. Efficient one pass self-distillation with zipf’s label smoothing. In *European Conference on Computer Vision (ECCV)*, pages 104–119. Springer, 2022.

K. Lyu and J. Li. Gradient descent maximizes the margin of homogeneous neural networks. In *International Conference on Learning Representations (ICLR)*, 2020. URL <https://arxiv.org/abs/1906.05890>.

F. Mignacco, F. Krzakala, L. Zdeborová, et al. The role of regularization in classification of high-dimensional noisy gaussian mixture. In *Proceedings of the 37th International Conference on Machine Learning (ICML)*, 2020.

A. Montanari, F. Ruan, Y. Sohn, and J. Yan. The generalization error of max-margin linear classifiers: High-dimensional asymptotics in the overparameterized regime. *arXiv preprint arXiv:1911.01544*, 2019. URL <https://arxiv.org/abs/1911.01544>.

R. Müller, S. Kornblith, and G. E. Hinton. When does label smoothing help? In *Advances in Neural Information Processing Systems (NeurIPS)*, 2019. URL <https://arxiv.org/abs/1906.02629>.

V. Petyan, X. Han, and D. L. Donoho. Prevalence of neural collapse during the terminal phase of deep learning training. *Proceedings of the National Academy of Sciences*, 2020. URL <https://arxiv.org/abs/2008.08186>.

G. Pereyra, G. Tucker, J. Chorowski, Ł. Kaiser, and G. Hinton. Regularizing neural networks by penalizing confident output distributions. *arXiv preprint arXiv:1701.06548*, 2017.

A. Power, Y. Burda, H. Edwards, I. Babuschkin, and V. Misra. Grokking: Generalization beyond overfitting on small algorithmic datasets. *arXiv preprint arXiv:2201.02177*, 2022. URL <https://arxiv.org/abs/2201.02177>.

L. Prieto, M. Barsbey, P. A. M. Mediano, and T. Birdal. Grokking at the edge of numerical stability, 2025. URL <https://arxiv.org/abs/2501.04697>.

Z. Shen, Z. Liu, D. Xu, Z. Chen, K.-T. Cheng, and M. Savvides. Is label smoothing truly incompatible with knowledge distillation: An empirical study. *arXiv preprint arXiv:2104.00676*, 2021.

D. Soudry, E. Hoffer, M. S. Nacson, S. Gunasekar, and N. Srebro. The implicit bias of gradient descent on separable data. *Journal of Machine Learning Research*, 19(70):1–57, 2018. URL <https://arxiv.org/abs/1710.10345>.

P. Súkeník, M. Mondelli, and C. Lampert. Neural collapse versus low-rank bias: Is deep neural collapse really optimal? *arXiv preprint arXiv:2405.14468*, 2024.

P. Sur and E. J. Candès. A modern maximum-likelihood theory for high-dimensional logistic regression. In *Proceedings of the National Academy of Sciences*, 2019. URL <https://arxiv.org/abs/1701.05023>.

C. Szegedy, V. Vanhoucke, S. Ioffe, J. Shlens, and Z. Wojna. Rethinking the inception architecture for computer vision. In *Proceedings of the IEEE/CVF Conference on Computer Vision and Pattern Recognition (CVPR)*, pages 2818–2826, 2016.

A. N. Tikhonov and V. Y. Arsenin. Solutions of ill-posed problems. 1977. URL <https://api.semanticscholar.org/CorpusID:122072756>.

K. Wang and C. Thrampoulidis. Binary classification of gaussian mixtures: Abundance of support vectors, robustness, and generalization. *SIAM Journal on Mathematics of Data Science*, 2022. URL <https://arxiv.org/abs/2010.00000>.

H. Wei, R. Xie, H. Cheng, L. Feng, B. An, and Y. Li. Mitigating neural network overconfidence with logit normalization, 2022. URL <https://arxiv.org/abs/2205.09310>.

G. Xia, O. Laurent, G. Franchi, and C.-S. Bouganis. Towards understanding why label smoothing degrades selective classification and how to fix it. In *International Conference on Learning Representations (ICLR)*, 2025.

J. Xu and H. Liu. Quantifying the variability collapse of neural networks. In *Proceedings of the International Conference on Machine Learning (ICML)*, pages 38535–38550. PMLR, 2023.

L. Yuan, F. E. Tay, G. Li, T. Wang, and J. Feng. Revisiting knowledge distillation via label smoothing regularization. In *Proceedings of the IEEE/CVF Conference on Computer Vision and Pattern Recognition (CVPR)*, pages 3903–3911, 2020.

C.-B. Zhang, P.-T. Jiang, Q. Hou, Y. Wei, Q. Han, Z. Li, and M.-M. Cheng. Delving deep into label smoothing. *IEEE Transactions on Image Processing*, 30:5984–5996, 2021.

J. Zhou, C. You, X. Li, K. Liu, S. Liu, Q. Qu, and Z. Zhu. Are all losses created equal: A neural collapse perspective. *Advances in Neural Information Processing Systems (NeurIPS)*, 35:31697–31710, 2022.

F. Zhu, Z. Cheng, X.-Y. Zhang, and C.-L. Liu. Rethinking confidence calibration for failure prediction. In *European Conference on Computer Vision (ECCV)*, pages 518–536. Springer, 2022.

Appendices

A. Additional Related Work

Label smoothing and soft-target training. Label smoothing (LS) was introduced as “label-smoothing regularization” by Szegedy et al. (2016) and is now a standard tool for improving generalization and calibration in classification and sequence models (Müller et al., 2019; Guo et al., 2017). LS has been analyzed across domains, including neural machine translation (Gao et al., 2020). More broadly, LS is one instance of training with *soft targets*, closely related to knowledge distillation (Hinton et al., 2015; Yuan et al., 2020). The interaction between LS and distillation is nuanced, with studies investigating when LS-trained teachers help or harm KD (Shen et al., 2021; Chandrasegaran et al., 2022). Beyond fixed uniform smoothing, variants adapt the target distribution during training, including Online Label Smoothing (Zhang et al., 2021), Zipf label smoothing (Liang et al., 2022), and adaptive/self-knowledge smoothing (Lee et al., 2022). LS has also been linked to changes in feature geometry (Müller et al., 2019; Kornblith et al., 2021) and quantified via feature-variability measures (Xu and Liu, 2023). However, LS can be problematic for selective classification or failure prediction, motivating targeted fixes (Zhu et al., 2022; Xia et al., 2025).

Logit/output regularization beyond classic label smoothing. Methods that regularize the *logits* directly include entropy penalties (Pereyra et al., 2017), logit-norm regularizers (Dauphin and Cubuk, 2021), and logit normalization (Wei et al., 2022). A key theme is whether the loss remains *lower bounded* and admits a *finite* per-sample optimum, as in convex logit penalties, versus cross-entropy whose infimum is achieved only at infinite margin.

Implicit bias of cross-entropy and margin maximization. For separable linear classification, gradient descent on unregularized cross-entropy converges to the hard-margin SVM (Soudry et al., 2018). This has been extended to nonseparable data (Ji and Telgarsky, 2019) and overparameterized homogeneous models (Lyu and Li, 2020). Convex logit regularization provides a sharp contrast by forcing the per-sample objective to attain a finite minimum.

High-dimensional solvable models. Our analysis connects to classical work on the combinatorial “capacity” of linear separators (Cover, 1965; Gardner, 1988). Recent work develops precise high-dimensional asymptotics for max-margin classifiers via CGMT/AMP techniques (Montanari et al., 2019; Deng et al., 2019; Mignacco et al., 2020; Wang and Thrampoulidis, 2022). In related directions, high-dimensional logistic regression exhibits phase-transition phenomena tied to the existence of maximum-likelihood estimators (Sur and Candès, 2019; Celentano et al., 2021).

Grokking and delayed generalization. Grokking was popularized in neural networks trained on small algorithmic datasets (Power et al., 2022). Solvable models have since been developed for linear estimators (Levi et al., 2024) and logistic regression near the edge of separability (Beck et al., 2025). Logit regularization in this context was briefly discussed in Prieto et al. (2025); we identify an analogous delayed generalization region with a shifted threshold.

Simplex geometry and neural collapse. Our multi-class setup relates to the *neural collapse* phenomenon (Papyan et al., 2020; Han et al., 2022), where logits converge to structured simplex/ETF configurations. Recent work studies how different losses shape this collapse (Zhou et al., 2022; Guo et al., 2024) and how it interacts with low-rank bias (Súkeník et al., 2024; Garrod and Keating, 2025).

B. Label smoothing as a special case of logit regularization

We show that label smoothing (LS) can be written as a convex *logit regularizer* added to cross-entropy, matching our form $\ell = (1 - \alpha)\ell_{\text{CE}} + \alpha f$ (up to a reparameterization of α and additive constants).

Binary classification

Consider a two-class softmax. Let $t \equiv yz$ be the signed logit, so that $p_y = \sigma(t) = 1/(1 + e^{-t})$ and $p_{-y} = 1 - p_y = \sigma(-t)$. Standard cross-entropy is $\ell_{\text{CE}}(t) = -\log p_y = \log(1 + e^{-t})$. Binary LS with smoothing ε uses targets $(1 - \varepsilon, \varepsilon)$ and yields

$$\ell_{\text{LS}}(t) = -(1 - \varepsilon) \log p_y - \varepsilon \log p_{-y} = (1 - \varepsilon) \log(1 + e^{-t}) + \varepsilon \log(1 + e^t). \quad (10)$$

Using $\log(1 + e^t) + \log(1 + e^{-t}) = \log(2 + 2 \cosh t)$, we rewrite

$$\ell_{\text{LS}}(t) = (1 - 2\varepsilon) \ell_{\text{CE}}(t) + \varepsilon \log(2 + 2 \cosh t). \quad (11)$$

Thus, in the binary case LS is equivalent to logit regularization with

$$f_{\text{LS}}(t) = \frac{1}{2} \log(2 + 2 \cosh t), \quad t = yz, \quad (12)$$

(up to rescaling $\alpha = 2\varepsilon$).

Multiclass classification

Let $p_k(\mathbf{z}) = \exp(z_k) / \sum_j \exp(z_j)$ and one-hot labels $y_k \in \{0, 1\}$. LS replaces $y_k^{\text{LS}} = (1 - \varepsilon)y_k + \varepsilon/K$, giving

$$\begin{aligned} \mathcal{L}_{\text{LS}}(\mathbf{z}, \mathbf{y}) &= - \sum_{k=1}^K y_k^{\text{LS}} \log p_k(\mathbf{z}) \\ &= (1 - \varepsilon) \mathcal{L}_{\text{CE}}(\mathbf{z}, \mathbf{y}) + \frac{\varepsilon}{K} \sum_{k=1}^K [-\log p_k(\mathbf{z})]. \end{aligned} \quad (13)$$

Hence LS is of the form $(1 - \alpha)\mathcal{L}_{\text{CE}} + \alpha f(\mathbf{z})$ with the convex, permutation-symmetric logit regularizer

$$f_{\text{LS}}(\mathbf{z}) = \log \left(\sum_{k=1}^K e^{z_k} \right) - \frac{1}{K} \sum_{k=1}^K z_k, \quad (14)$$

C. Complementary details for Sec. 3.4

In Sec. 3.4 we showed that under some assumptions, the direction of the weight vector becomes almost invariant to the logit-regularization function in general, and in particular to the regularization strength α . We did by proving Proposition 3.1 and Corollary 3.2, where we showed if the distribution of the data is strictly gaussian, this will be true for any convex per-sample loss, and on the other hand if the per-sample loss is quadratic, then it will be true regardless of its minimum.

C.1. Complementary proofs

We begin by proving a Lemma which is needed for the proof of Proposition 3.1.

Lemma C.1. *Let x be a zero-mean random variable and let $f : \mathbb{R} \rightarrow \mathbb{R}$ be a convex function. Then $\mathbb{E}[f(\lambda x)]$ is an nondecreasing function of λ for $\lambda > 0$.*

Proof. This is a standard convexity argument. Let's examine two lambdas $0 < \lambda_1 < \lambda_2$. Then λ_1 is a convex combination of 0 and λ_2 ,

$$\lambda_1 = \left(1 - \frac{\lambda_1}{\lambda_2}\right) \cdot 0 + \frac{\lambda_1}{\lambda_2} \lambda_2.$$

Therefore,

$$\begin{aligned} \mathbb{E}[f(\lambda_1 x)] &= \mathbb{E} \left[f \left(\left(1 - \frac{\lambda_1}{\lambda_2}\right) \cdot 0 + \frac{\lambda_1}{\lambda_2} \lambda_2 x \right) \right] \\ &\leq \left(1 - \frac{\lambda_1}{\lambda_2}\right) f(0) + \frac{\lambda_1}{\lambda_2} \mathbb{E}[f(\lambda_2 x)] \\ &\leq \mathbb{E} \left[\left(1 - \frac{\lambda_1}{\lambda_2}\right) f(\lambda_2 x) + \frac{\lambda_1}{\lambda_2} f(\lambda_2 x) \right] = \mathbb{E}[f(\lambda_2 x)] \end{aligned}$$

Where we used the fact that x is zero-mean and therefore $f(0) = f(\mathbb{E}[\lambda_2 x]) \leq \mathbb{E}[f(\lambda_2 x)]$. \square

The connection to Proposition 3.1: For fixed $\mu \in \mathbb{R}$, define $g(t) \equiv f(\mu + t)$, which is convex whenever f is convex. Applying Lemma C.1 with $x = Y \sim \mathcal{N}(0, 1)$ yields that

$$Q(\mu, \sigma) = \mathbb{E}[f(\mu + \sigma Y)] = \mathbb{E}[g(\sigma Y)]$$

is nondecreasing in $\sigma \geq 0$ for each fixed μ .

We will now provide the proof to Corollary 3.3 in the main text.

Theorem C.2 (Restatement of Corollary 3.3). *If the data is Gaussian, the optimal weight direction is $\hat{\mathbf{S}}_{\min} \propto \Sigma^{-1}\mu$ and therefore independent of the convex regularization function f . Similarly, if $\lambda = d/N < 1$ and the per-sample loss is quadratic, $\hat{\mathbf{S}}_{\min} \propto \Sigma^{-1}\mu$ (where Σ, μ are the empirical mean and centered covariance) and therefore independent of the target value z^* .*

Proof. **Population Gaussian.** For $\mathbf{x} \sim \mathcal{N}(\mu, \Sigma)$ and any \mathbf{S} , the logit $z = \mathbf{S}^\top \mathbf{x}$ is Gaussian with mean $\mu(\mathbf{S}) = \mathbf{S}^\top \mu$ and variance $\sigma^2(\mathbf{S}) = \mathbf{S}^\top \Sigma \mathbf{S}$. By Proposition 3.1, any minimizer of $L(\mathbf{S}) = \mathbb{E}[\ell(z)]$ minimizes the ratio $r(\mathbf{S}) = \sigma(\mathbf{S})/\mu(\mathbf{S})$ over $\{\mu(\mathbf{S}) > 0\}$, i.e.

$$r(\mathbf{S})^2 = \frac{\mathbf{S}^\top \Sigma \mathbf{S}}{(\mathbf{S}^\top \mu)^2}.$$

Using Cauchy–Schwarz,

$$(\mathbf{S}^\top \mu)^2 = \langle \Sigma^{1/2} \mathbf{S}, \Sigma^{-1/2} \mu \rangle^2 \leq (\mathbf{S}^\top \Sigma \mathbf{S}) (\mu^\top \Sigma^{-1} \mu),$$

hence $r(\mathbf{S})^2 \geq (\mu^\top \Sigma^{-1} \mu)^{-1}$. Moreover, equality holds iff $\Sigma^{1/2} \mathbf{S} \propto \Sigma^{-1/2} \mu$, equivalently $\mathbf{S} \propto \Sigma^{-1} \mu$.

Empirical quadratic. Let $\ell(z) = a(z - z^*)^2$ and define $\hat{\mu} = \frac{1}{N} \sum_i \mathbf{x}_i$, $\hat{\Sigma} = \frac{1}{N} \sum_i (\mathbf{x}_i - \hat{\mu})(\mathbf{x}_i - \hat{\mu})^\top$. Assume that Σ is invertible (since $\lambda < 1$), then

$$\hat{L}(\mathbf{S}) = \frac{a}{N} \sum_i (\mathbf{S}^\top \mathbf{x}_i - z^*)^2 = a \mathbf{S}^\top \hat{\Sigma} \mathbf{S} + a(\mathbf{S}^\top \hat{\mu} - z^*)^2,$$

so the optimal *direction* minimizes $\hat{r}(\mathbf{S})^2 = \frac{\mathbf{S}^\top \hat{\Sigma} \mathbf{S}}{(\mathbf{S}^\top \hat{\mu})^2}$ and is independent of z^* . Repeating the Cauchy–Schwarz step from the Gaussian case gives the result. \square

C.2. Additional numerical evidence

We numerically illustrate the finite-sample mechanism behind the α -plateau discussed in Sec. 3.4. For each N , we sample $\mathbf{x}_i \in \mathbb{R}^2$ i.i.d. from a Gaussian and compute the empirical minimizer

$$S_{\min}(\alpha) = \arg \min_{\mathbf{S}} \frac{1}{N} \sum_{i=1}^N \left[(1 - \alpha) \log(1 + e^{-\mathbf{x}_i^\top \mathbf{S}}) + \alpha(\mathbf{x}_i^\top \mathbf{S})^2 \right].$$

As a reference direction, we also compute S_{\min}^{quad} for the purely quadratic per-sample loss $b(z - a)^2$ on the same dataset (with values $b = a = 1$, but we also verified that it does not matter what are these values from Corollary 3.2), and plot $\tan \theta(\alpha)$ where $\theta(\alpha)$ is the angle between $S_{\min}(\alpha)$ and S_{\min}^{quad} .

Figure 10 shows that for small N , $S_{\min}(\alpha)$ can deviate at very small α (finite-sample non-Gaussianity), but it stabilizes for large α as the objective becomes effectively quadratic. For larger N , the plateau is reached at much smaller α , consistent with improved approximate Gaussianity.

Two toy examples with $N = 3$ points. We next give two minimal $N = 3$ demonstrations that separate the “quadratic invariance” mechanism from the “Gaussian-logit” mechanism.

Figure 11: changing a only (quadratic case). We sample three points $\mathbf{x}_1, \mathbf{x}_2, \mathbf{x}_3 \in \mathbb{R}^2$ in random position and minimize

$$\frac{1}{3} \sum_{i=1}^3 \ell(z_i), \quad z_i = \mathbf{S}^\top \mathbf{x}_i, \quad \ell(z) = (z - a)^2 + b \max(0, -z).$$

In the first toy example we set $b = 0$, so the objective is purely quadratic in z . We compare two runs with $(a, b) = (2, 0)$ and $(a, b) = (6, 0)$. As shown in Figure 11, the minimizers S_1^{\min} and S_2^{\min} point in exactly the same direction and differ only by a scalar factor (left panel). Accordingly, the three logits $z_i = \mathbf{S}^\top \mathbf{x}_i$ shift to different absolute values between the two runs (right panel), but their “clustering ratio”

$$r = \frac{\sigma}{\mu}$$

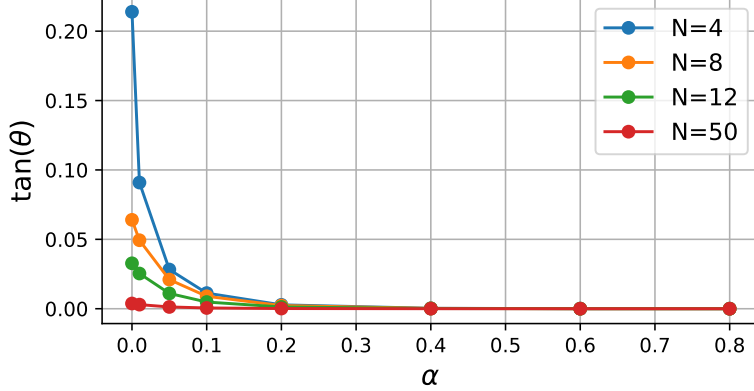


Figure 10. **Finite-sample α -plateau.** $\tan \theta(\alpha)$ between $S_{\min}(\alpha)$ for $(1 - \alpha) \log(1 + e^{-z}) + \alpha z^2$ and the reference direction S_{\min}^{quad} for $b(z - a)^2$, for several N . Small N shows deviations at small α . Increasing N makes the plateau appear at even smaller α . Note that the smallest α in this figure is $\alpha = 0.00001$.

(where μ and σ are the empirical mean and standard deviation over the three logits) remains constant: we report (μ, σ, r) in the table in the bottom row of the figure. This is a direct finite-sample illustration of the direction-independence in the quadratic regime (Corollary 3.2): changing the quadratic target a rescales the minimizer without changing its direction.

Figure 12: adding a hinge-like term (non-quadratic, non-Gaussian). In the second toy example we keep $a = 2$ fixed and compare $(a, b) = (2, 0)$ versus $(a, b) = (2, 6)$. Now the objective includes the non-quadratic term $b \max(0, -z)$, and with only three points the induced logit distribution is extremely far from Gaussian. In this setting, neither of the sufficient conditions underlying our invariance arguments holds (quadratic loss or Gaussian logit distribution), and we indeed observe that the two minimizers are no longer perfectly colinear (though their angle remains moderate); see Figure 12.

The invariance to α in the case of the Gaussian model. In Figure 13 we show that for when the data is taken from Gaussian distribution, the direction is almost flat as a function of α , even for small values. We show it for different values of $\lambda = d/N$. The slight deviation from the plateau is expected from finite-sampling effects.

C.3. Alternative proof of Proposition 3.1 via monotonicity of $Q(r)$

We provide an equivalent proof based on defining an objective $Q(r)$ directly and showing it is strictly increasing in the coefficient of variation r .

Proposition C.3 (Restatement of Proposition 3.1 for convenience). *Let $\mathbf{x} \in \mathbb{R}^d$ be Gaussian, $\mathbf{x} \sim \mathcal{N}(\boldsymbol{\mu}_x, \Sigma_x)$ with $\boldsymbol{\mu}_x \neq 0$. Let $f : \mathbb{R} \rightarrow \mathbb{R}$ be convex, twice differentiable, and with a unique minimizer at $m > 0$. For $\mathbf{S} \in \mathbb{R}^d$ define the logit*

$$z = \mathbf{S}^\top \mathbf{x} \sim \mathcal{N}(\mu, \sigma^2), \quad \mu(\mathbf{S}) = \mathbf{S}^\top \boldsymbol{\mu}_x, \quad \sigma^2(\mathbf{S}) = \mathbf{S}^\top \Sigma_x \mathbf{S},$$

and the population objective $L(\mathbf{S}) = \mathbb{E}[f(z)]$. Then any minimizer $\mathbf{S}_{\min} \in \arg \min_{\mathbf{S}} L(\mathbf{S})$ also minimizes the ratio

$$r(\mathbf{S}) = \frac{\sigma(\mathbf{S})}{\mu(\mathbf{S})} \quad \text{over all } \mathbf{S} \text{ such that } \mu(\mathbf{S}) > 0.$$

Proof. Write $\hat{\mathbf{S}} = \mathbf{S}/\|\mathbf{S}\|$ and define

$$\hat{z} = \hat{\mathbf{S}}^\top \mathbf{x} \sim \mathcal{N}(\hat{\mu}, \hat{\sigma}^2), \quad \hat{\mu} = \hat{\mathbf{S}}^\top \boldsymbol{\mu}_x, \quad \hat{\sigma}^2 = \hat{\mathbf{S}}^\top \Sigma_x \hat{\mathbf{S}}.$$

We first note that any minimizing direction must satisfy $\hat{\mu} > 0$. Fix a unit direction $\hat{\mathbf{S}}$ and consider the one-dimensional restriction

$$h(t) = \mathbb{E}[f(t \hat{z})], \quad t = \|\mathbf{S}\| \geq 0.$$

By convexity of f , h is convex in t , and $h(0) = f(0)$ with

$$h'(0) = \mathbb{E}[f'(0) \hat{z}] = \hat{\mu} f'(0).$$

$$f(z) = (z - a)^2 + b * \max(0, -z)$$

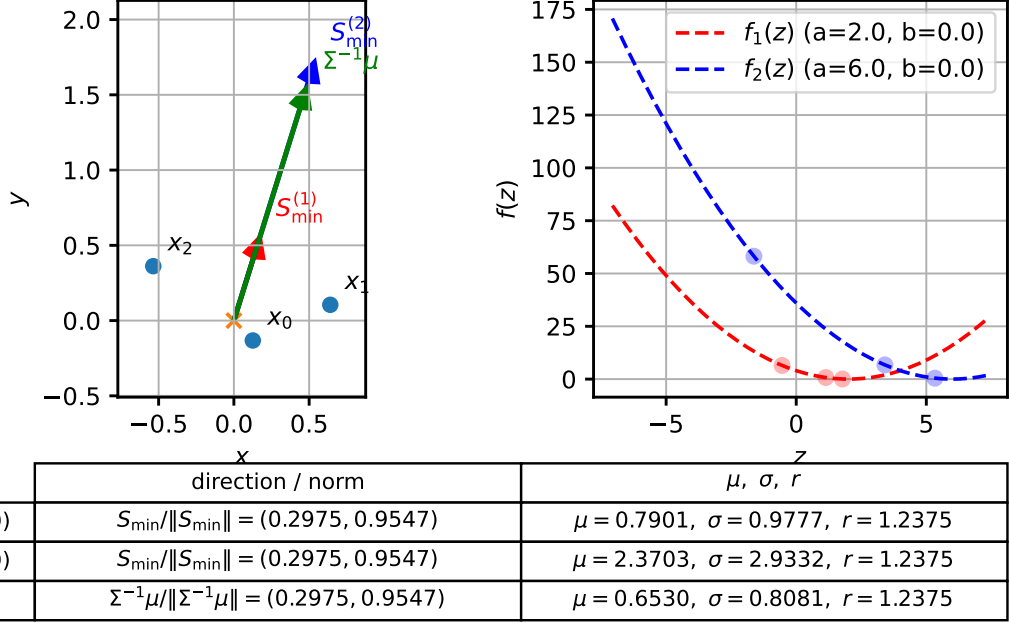


Figure 11. Toy example ($N = 3$) with a quadratic loss: changing a rescales the minimizer but does not change its direction. We minimize $\frac{1}{3} \sum_{i=1}^3 (S^\top x_i - a)^2$ over $S \in \mathbb{R}^2$ for two choices of a (here $a = 2$ and $a = 6$, with $b = 0$). We also present for comparison the direction $\Sigma^{-1}\mu$. **Left:** the three points x_1, x_2, x_3 and the two minimizers S_1^{\min}, S_2^{\min} , which are colinear. **Right:** the corresponding logits $\{S^\top x_i\}_{i=1}^3$ for both runs (shown in different colors), which shift in absolute value. **Bottom:** empirical μ (mean), σ (std), and $r = \sigma/\mu$, showing that the coefficient of variation is unchanged across the two runs.

Since f has a unique minimizer at $m > 0$, convexity implies $f'(0) < 0$. If $\hat{\mu} < 0$, then $h'(0) > 0$ and by convexity h is minimized at $t = 0$. If $\hat{\mu} > 0$, then $h'(0) < 0$ and h attains its unique minimizer at some $t > 0$. Thus, flipping $\hat{S} \mapsto -\hat{S}$ strictly improves the loss near the origin whenever $\hat{\mu} < 0$, so every minimizing direction must satisfy $\hat{\mu} > 0$.

Assume henceforth $\mu(S) > 0$. Let $Y \sim \mathcal{N}(0, 1)$ so that

$$z = \mu + \sigma Y = \mu(1 + rY), \quad r = \frac{\sigma}{\mu}.$$

Define

$$q(\mu, r) = \mathbb{E}[f(\mu(1 + rY))], \quad \mu > 0, r \geq 0.$$

For a fixed direction \hat{S} , scaling S by a positive factor scales both μ and σ by the same factor, hence leaves $r = \sigma/\mu$ invariant. Therefore,

$$L_{\min} = \min_{\hat{S}} \min_{\mu > 0} q(\mu, r(\hat{S})).$$

Define the reduced objective

$$Q(r) = \min_{\mu > 0} q(\mu, r),$$

so that

$$L_{\min} = \min_{\hat{S}} Q(r(\hat{S})).$$

It suffices to show Q is strictly increasing on $(0, \infty)$. Let $\mu^*(r)$ be a minimizer of $q(\mu, r)$ over $\mu > 0$, so $Q(r) = q(\mu^*(r), r)$. Differentiating and using $\partial_\mu q(\mu^*(r), r) = 0$ at the optimum (envelope theorem), we obtain

$$\frac{dQ}{dr} = \frac{\partial q}{\partial r}(\mu^*(r), r) = \mu^*(r) \mathbb{E}[f'(\mu^*(r)(1 + rY)) Y].$$

$$f(z) = (z - a)^2 + b * \max(0, -z)$$

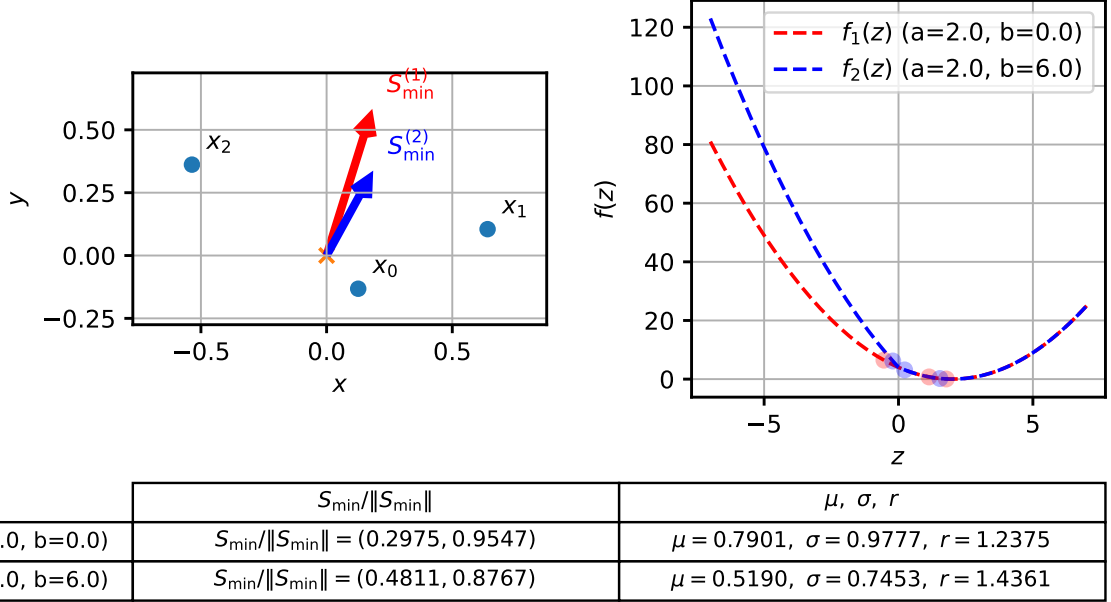


Figure 12. Toy example ($N = 3$) where invariance need not hold: adding a hinge-like term changes the direction. We minimize $\frac{1}{3} \sum_{i=1}^3 [(S^\top x_i - a)^2 + b \max(0, -S^\top x_i)]$ for two settings: $(a, b) = (2, 0)$ and $(a, b) = (2, 6)$ on the same three points. Because the loss is no longer purely quadratic and the empirical logit distribution (with $N = 3$) is far from Gaussian, the two minimizers need not share the same direction, and we observe a noticeable (but not extreme) angular deviation between them.

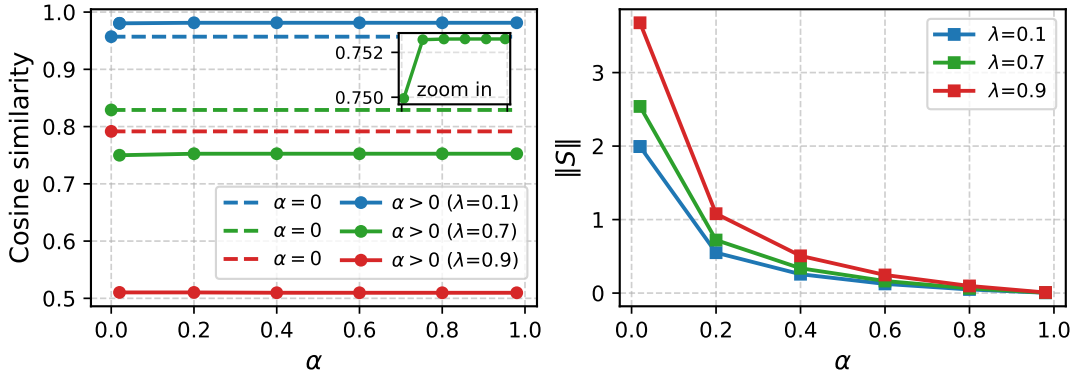


Figure 13. **Left panel:** Cosine similarity of \mathbf{S}_{\min} with the x-axis. The dashed line indicates the unregularized value ($\alpha = 0$). We observe an abrupt shift from $\alpha = 0$ to $\alpha > 0$, followed by a stable plateau, indicating that the weight direction is effectively independent of α . **Right panel:** The norm $\|\mathbf{S}_{\min}\|$, which, in contrast, exhibits a clear dependence on α .

Using Gaussian integration by parts, $\mathbb{E}[g(Y)Y] = \mathbb{E}[g'(Y)]$ for $Y \sim \mathcal{N}(0, 1)$, with $g(y) = f'(\mu^*(1 + ry))$ and $g'(y) = r\mu^*f''(\mu^*(1 + ry))$, yields

$$\mathbb{E}[f'(\mu^*(1 + rY))Y] = r\mu^* \mathbb{E}[f''(\mu^*(1 + rY))].$$

Hence

$$\frac{dQ}{dr} = r\mu^*(r)^2 \mathbb{E}[f''(\mu^*(r)(1 + rY))].$$

For $r > 0$, $\mu^*(r) > 0$, and convex f we have $f'' \geq 0$ (and > 0 a.e. if f is strictly convex), so $\frac{dQ}{dr} > 0$ for all $r > 0$. Therefore Q is increasing in r , and the minimizing direction must achieve the smallest attainable $r(\hat{\mathbf{S}}) = \hat{\sigma}/\hat{\mu}$. Equivalently,

any $\mathbf{S}_{\min} \in \arg \min_{\mathbf{S}} L(\mathbf{S})$ minimizes $r(\mathbf{S}) = \sigma(\mathbf{S})/\mu(\mathbf{S})$ over $\mu(\mathbf{S}) > 0$. \square

C.4. Explicit Derivation for the Quadratic Case

To build intuition, we consider the pedagogically illuminating case where the per-sample loss is purely quadratic, $\ell(z) = (z - a)^2$. In this setting, we can derive the optimal weight vector explicitly and demonstrate directly that minimizing the loss is equivalent to minimizing the coefficient of variation r .

Suppose that the loss is :

$$\mathcal{L}(\mathbf{S}) = \mathbb{E}[(z - a)^2], \quad (15)$$

where $z = \mathbf{S}^T \mathbf{x}$. Let the direction of the weights be $\hat{\mathbf{S}} = \mathbf{S}/\|\mathbf{S}\|$ and the norm be $g = \|\mathbf{S}\|$. We denote the unit-direction moments as $\hat{\mu} = \mathbb{E}[\hat{\mathbf{S}} \cdot \mathbf{x}]$ and $\hat{\sigma}^2 = \text{Var}(\hat{\mathbf{S}} \cdot \mathbf{x})$. The statistics of the full logit are then $\mu = g\hat{\mu}$ and $\sigma = g\hat{\sigma}$.

Using the bias-variance decomposition $\mathbb{E}[(z - a)^2] = \text{Var}(z) + (\mathbb{E}[z] - a)^2$, the loss becomes:

$$\mathcal{L}(g, \hat{\mathbf{S}}) \approx \sigma^2 + (\mu - a)^2 = g^2 \hat{\sigma}^2 + (g\hat{\mu} - a)^2. \quad (16)$$

We first optimize the scale g for a fixed direction $\hat{\mathbf{S}}$. Taking the derivative with respect to g :

$$\frac{\partial \mathcal{L}}{\partial g} = 2g\hat{\sigma}^2 + 2(g\hat{\mu} - a)\hat{\mu} = 0. \quad (17)$$

Solving for g , we obtain the optimal norm:

$$g^* = a \frac{\hat{\mu}}{\hat{\mu}^2 + \hat{\sigma}^2}. \quad (18)$$

Substituting this back into the expression for the mean logit $\mu^* = g^* \hat{\mu}$, we find:

$$\mu^* = a \frac{\hat{\mu}^2}{\hat{\mu}^2 + \hat{\sigma}^2} = \frac{a}{1 + r^2}, \quad (19)$$

where $r = \hat{\sigma}/\hat{\mu} = \sigma/\mu$ is the clustering ratio. This reveals a shrinkage effect: the optimal mean μ^* is slightly *smaller* than the target a to reduce the variance penalty.

Finally, substituting g^* back into the loss function yields the minimal loss achievable for the direction $\hat{\mathbf{S}}$:

$$\mathcal{L}_{\min}(\hat{\mathbf{S}}) = g^{*2} \hat{\sigma}^2 + (g^* \hat{\mu} - a)^2 = a^2 \frac{\hat{\sigma}^2}{\hat{\mu}^2 + \hat{\sigma}^2} = a^2 \frac{1}{1 + 1/r^2}. \quad (20)$$

Therefore, minimizing the total loss is mathematically equivalent to minimizing the coefficient of variation r .

D. Complementary details for Sec. 7 (Multi-class classification)

In this section we will provide complementary details for the multiclass case. We will show that most of the results generalize naturally.

D.1. Logit clustering

We consider a K -class linear classifier $\mathbf{z} = \mathbf{W}\mathbf{x} + \mathbf{b}$. As discussed in the main text, when adding convex and symmetric logit-regularization function $f(\mathbf{z})$, the loss in the multi-class case can also be decomposed as a sum of per-sample loss functions. The main difference is that now, each class has a different per-sample minimum. The goal of the optimizer is to cluster all of the logits of a certain class to its corresponding minimum, and hence the implicit bias would be, again, logit clustering. From symmetry, this minimum should take the form

$$\mathbf{z}_{c,k}^* = \begin{cases} q_{\text{high}} & k = c \\ q_{\text{low}} & \text{else} \end{cases} \quad (21)$$

where $k = 1, \dots, K$ is the class index, c is the class of the logit (determined by the label), and $q_{\text{high}} > q_{\text{low}}$ are some scalars. We will begin by considering a quadratic loss, and showing that the "direction" and optimal generalization accuracy is invariant to its specific details.

D.2. Invariance to the Quadratic Logit Regularization Function

We generalize Corollary 3.2 to the multi-class setting. Assuming that the per-sample loss function is quadratic *around the corresponding class minimum*, we show that generalization accuracy is invariant to the specific target values (and thus the regularization parameters).

Proposition D.1 (Quadratic Loss Invariance). *Consider a multi-class linear classifier minimizing the empirical loss $\mathcal{L} = \frac{1}{N} \sum_i \ell(\mathbf{z}_i, \mathbf{y}_i)$, where the per-sample loss is quadratic:*

$$\ell(\mathbf{z}, \mathbf{y}_c) = |\mathbf{z} - \mathbf{z}_c^*|^2, \quad (22)$$

and $\mathbf{z}_c^* \in \mathbb{R}^K$ is a target vector specific to class c . Then, for any $q \neq 0$, the generalization accuracy of the optimal solution is invariant to the value of q .

Proof. Let $W \in \mathbb{R}^{K \times d}$ and $\mathbf{b} \in \mathbb{R}^K$. The logits are given by $\mathbf{z}_i = W\mathbf{x}_i + \mathbf{b}$. We notice that up to a global shift that can be compensated by the bias, we can assume that $q_{\text{low}} = 0$. Therefore, $\mathbf{z}_c^* = q\mathbf{e}_c$. The loss function is:

$$\mathcal{L}(W, \mathbf{b}) = \frac{1}{N} \sum_{i=1}^N |\mathbf{z}_i - q\mathbf{y}_i|^2, \quad (23)$$

where \mathbf{y}_i is the one-hot representation of the label. We can factor out q^2 :

$$\mathcal{L}(W, \mathbf{b}) = q^2 \frac{1}{N} \sum_i \left| \left(\frac{1}{q} W \right) \mathbf{x}_i + \left(\frac{1}{q} \mathbf{b} \right) - \mathbf{y}_i \right|^2. \quad (24)$$

Let $\tilde{W} = W/q$ and $\tilde{\mathbf{b}} = \mathbf{b}/q$. Minimizing \mathcal{L} with respect to W, \mathbf{b} is equivalent to minimizing the term inside the summation with respect to $\tilde{W}, \tilde{\mathbf{b}}$. Let $\tilde{W}_{\min}, \tilde{\mathbf{b}}_{\min}$ be the minimizers for the case $q = 1$. Then the minimizers for an arbitrary q are simply $W_{\min} = q\tilde{W}_{\min}$ and $\mathbf{b}_{\min} = q\tilde{\mathbf{b}}_{\min}$. The predicted class for a test point \mathbf{x} is:

$$\hat{y} = \underset{k}{\operatorname{argmax}} (W_{\min} \mathbf{x} + \mathbf{b}_{\min})_k = \underset{k}{\operatorname{argmax}} (q(\tilde{W}_{\min} \mathbf{x} + \tilde{\mathbf{b}}_{\min}))_k. \quad (25)$$

Since q is a positive scalar, the argmax (and thus the accuracy) remains unchanged. \square

In the binary setting (Proposition 3.1), the scalar coefficient of variation $r = \sigma/\mu$ is equivalent (up to inversion) to the LDA objective: maximizing μ/σ is the same as maximizing the Rayleigh quotient

$$J(\mathbf{S}) = \frac{(\mathbf{S}^\top \boldsymbol{\mu})^2}{\mathbf{S}^\top \Sigma \mathbf{S}},$$

whose maximizer is $\mathbf{S} \propto \Sigma^{-1} \boldsymbol{\mu}$. In the multi-class case, Fisher's criterion has a standard generalization obtained by replacing the scalar mean-variance ratio with a between-class versus within-class scatter ratio. Writing $\boldsymbol{\mu}_c$ for class means, $\boldsymbol{\mu}$ for the global mean, and defining the scatters

$$S_B = \sum_{c=1}^K \pi_c (\boldsymbol{\mu}_c - \boldsymbol{\mu})(\boldsymbol{\mu}_c - \boldsymbol{\mu})^\top, \quad (26)$$

the multi-class Fisher objective for a $(K-1)$ -dimensional projection $U \in \mathbb{R}^{d \times (K-1)}$ is

$$J(U) = \operatorname{tr} \left((U^\top S_W U)^{-1} U^\top S_B U \right) \quad (27)$$

(equivalently, $\det(U^\top S_B U) / \det(U^\top S_W U)$). This reduces to the binary μ/σ criterion when $K = 2$ and is maximized by the top $(K-1)$ generalized eigenvectors of the pair (S_B, S_W) (i.e., of $S_W^{-1} S_B$). Accordingly, the natural multi-class analogue of our scalar clustering invariant is the Fisher scatter ratio encoded by these generalized eigenvalues (or their sum/product), rather than a single σ/μ .

D.3. Shift of the Interpolation Threshold ($\sigma_f = 0$)

In this section, we provide the multi-class generalization for the shift of the interpolation threshold in the noiseless feature regime. We also demonstrate in Figure 8 that a grokking dynamics can be achieved, while also the fact that the logits cluster at a single point at the end of the training.

Proposition D.2. *Consider the multi-class model with $\alpha > 0$ and $\sigma_f = 0$. Assume the limit where $d, N \rightarrow \infty$ with $\lambda = d/N < 1$. Furthermore, assume that the class means $\{\mu_c\}_{c=1}^K \subset \mathbb{R}^d$ span a $(K-1)$ -dimensional affine subspace and are affinely independent. Then, the parameters W_{\min}, b_{\min} that minimize the training loss achieve perfect generalization accuracy.*

Proof. Since $\sigma_f = 0$, any sample $\mathbf{x}^{(i)}$ belonging to class c lies in a subspace defined by the class mean plus orthogonal noise:

$$\mathbf{x}^{(i)} = \mu_c + \xi_{\perp}^{(i)}, \quad (28)$$

where μ_c is the deterministic signal component, and $\xi_{\perp}^{(i)}$ lies in the orthogonal complement of the signal subspace $\mathcal{S} = \text{span}(\{\mu_k\})$. The regularized loss is a sum of strictly convex per-sample losses. A global lower bound for the total loss is achieved if and only if the logit vector for every sample i of class c coincides exactly with the unique minimizer of the class-specific per-sample loss, $\mathbf{z}_c^* \in \mathbb{R}^K$.

We decompose the weight matrix W into a component acting on the signal subspace, W_{sig} , and a component acting on the orthogonal noise, W_{\perp} . We construct a solution where $W_{\perp} = 0$. The condition for achieving the global minimum on the training set becomes:

$$W_{\text{sig}}\mu_c + b = \mathbf{z}_c^*, \quad \forall c \in \{1, \dots, K\}. \quad (29)$$

We can rewrite this using augmented notation. Let $\tilde{W}_{\text{sig}} = [\mathbf{b}, W_{\text{sig}}]$ and $\tilde{\mu}_c = [1, \mu_c^{\top}]^{\top}$. The system is:

$$\tilde{W}_{\text{sig}} M = Z^*, \quad (30)$$

where columns of M are the augmented means $\tilde{\mu}_c$, and columns of Z^* are the targets \mathbf{z}_c^* . Since the class means are affinely independent, the matrix $M \in \mathbb{R}^{K \times K}$ is invertible. Thus, a unique solution $\tilde{W}_{\text{sig}} = Z^* M^{-1}$ exists.

For $\lambda < 1$, the loss is strictly convex, ensuring this solution is unique. Thus, the learned weights map every sample (train or test) of class c exactly to \mathbf{z}_c^* . As \mathbf{z}_c^* minimizes the loss for label c , it must correctly classify the input so the classifier achieves 100% accuracy. \square

D.4. Invariance to Orthogonal Noise (σ_n)

Finally, we generalize Theorem 6.1 to the multi-class case.

Proposition D.3. *Let $\alpha > 0$ and $\lambda < 1$. In the multi-class setting described in Sec. 7, the generalization accuracy of the optimal classifier is independent of the orthogonal noise scale σ_n .*

Proof. Let the data for class c be $\mathbf{x} = \mathbf{x}_{\text{sig}} + \sigma_n \boldsymbol{\eta}_{\perp}$, where $\mathbf{x}_{\text{sig}} \in \mathcal{S}$ and $\boldsymbol{\eta}_{\perp} \in \mathcal{S}^{\perp}$. Decompose the weight matrix as $W = W_{\text{sig}} + W_{\perp}$, where the rows of W_{sig} lie in \mathcal{S} and rows of W_{\perp} lie in \mathcal{S}^{\perp} . The logits are:

$$\mathbf{z} = W_{\text{sig}} \mathbf{x}_{\text{sig}} + \sigma_n W_{\perp} \boldsymbol{\eta}_{\perp} + \mathbf{b}. \quad (31)$$

Let (W, \mathbf{b}) be the minimizer for noise scale σ_n . The loss depends on the logits \mathbf{z}_i . Consider a scaling of the noise $\sigma_n \rightarrow \beta \sigma_n$. The input noise becomes $\beta \sigma_n \boldsymbol{\eta}_{\perp}$. To maintain the same optimal logit values (and thus the same minimal loss value), the optimizer must scale the orthogonal weight component inversely: $W'_{\perp} = \frac{1}{\beta} W_{\perp}$. The term relevant for prediction on test data is the inner product of the noise and weights:

$$(\beta \sigma_n \boldsymbol{\eta}_{\perp})^{\top} (W'_{\perp})^{\top} = \beta \sigma_n \boldsymbol{\eta}_{\perp}^{\top} \left(\frac{1}{\beta} W_{\perp}^{\top} \right) = \sigma_n \boldsymbol{\eta}_{\perp}^{\top} W_{\perp}^{\top}. \quad (32)$$

This term is invariant to β . Since the signal term $W_{\text{sig}} \mathbf{x}_{\text{sig}}$ is unaffected by σ_n , the distribution of test logits remains identical. Consequently, the accuracy is invariant. \square

E. Supplemental numerical results

In this section we will present additional numerical results, supporting our results throughout the paper.

E.1. Discrepancy Between Training and Test Logit Distributions

Our geometric framework provides a mechanism explaining why test logits cluster less tightly than training logits. In the finite-data regime, the optimizer identifies a weight direction that minimizes the empirical variance of the *training* logits. This is often achieved by exploiting specific noise correlations to "over-cluster" the data — effectively reducing the empirical variance below the intrinsic population noise level. However, achieving this requires the learned weight vector to deviate from the true signal direction μ_f . This misalignment introduces a non-zero orthogonal component (S_{\perp}), which necessarily increases the variance of the test logits (which follow the population statistics). Consequently, the test clusters are looser than those observed during training, as demonstrated in Figure 14.

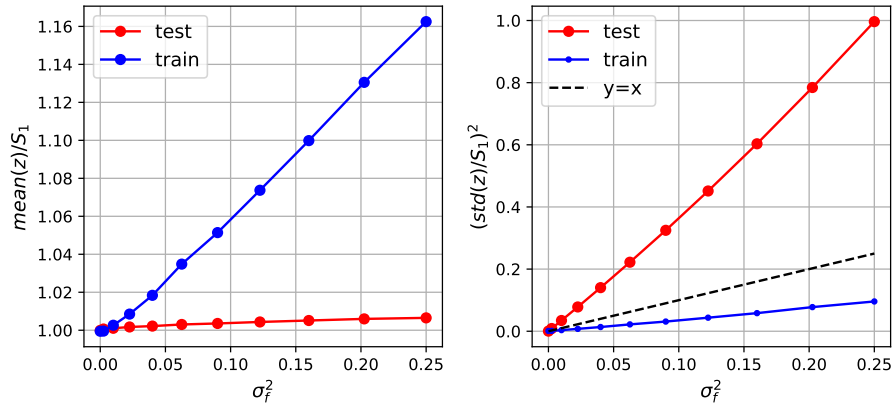


Figure 14. Logit statistics vs. signal noise σ_f . The mean and standard deviation of the logits in the binary classification setup are shown as functions of σ_f . The diagonal ($y = x$) serves as a reference for the intrinsic signal noise. **Test Set (Generalization):** The variance is given by $\sigma_z^2 = \sigma_f^2 S_1^2 + \sigma_n^2 \|S_{\perp}\|^2$. Due to the misalignment term $\|S_{\perp}\|^2$, the test standard deviation typically exceeds the signal contribution, lying above the reference line. **Training Set:** Conversely, the training standard deviation lies below the reference line. This indicates that the optimizer finds a specific direction that minimizes the training logit variance beyond the theoretical lower bound of the signal noise ($\sigma_z^2 S_1^2$). Here, $\lambda = d/N = 0.7$.

E.2. Phase Diagram of Logit Regularization Benefit

In the main text (Figure 6), we presented a phase diagram characterizing the regime where logit regularization improves generalization. That analysis focused on the separable setting ($\lambda = 0.7 > 1/2$). Here, we examine the nonseparable regime, $\lambda = 0.4 < 1/2$ (see Figure 15).

The primary distinction between these regimes lies in the behavior of the unregularized baseline as the orthogonal noise σ_n increases. In the overparameterized case ($\lambda > 1/2$), the training data is typically linearly separable due to the high dimensionality. Consequently, as σ_n grows, the unregularized max-margin solution aligns increasingly with the orthogonal noise directions rather than the signal feature. This causes the cosine similarity with the true feature axis to vanish, degrading the generalization accuracy toward random guessing (1/2).

In contrast, for $\lambda < 1/2$, the data is generally not linearly separable. Consequently, there is no "easy" overfitting solution that separates the training points using noise dimensions. Instead, increasing the amplitude of the noise will aid alignment: high orthogonal noise effectively drowns out spurious correlations, forcing the optimization to "tune" the margin toward 1 (see bottom panels of Figure 17). Therefore, rather than decaying to 1/2, we empirically observe that the accuracy of the unregularized solution saturates at a non-trivial constant value (see the left panel of Figure 15). This shift in asymptotic behavior alters the topology of the phase diagram. In general, the specific boundaries of the beneficial regime will depend on the geometric ratio λ and the underlying data distribution.

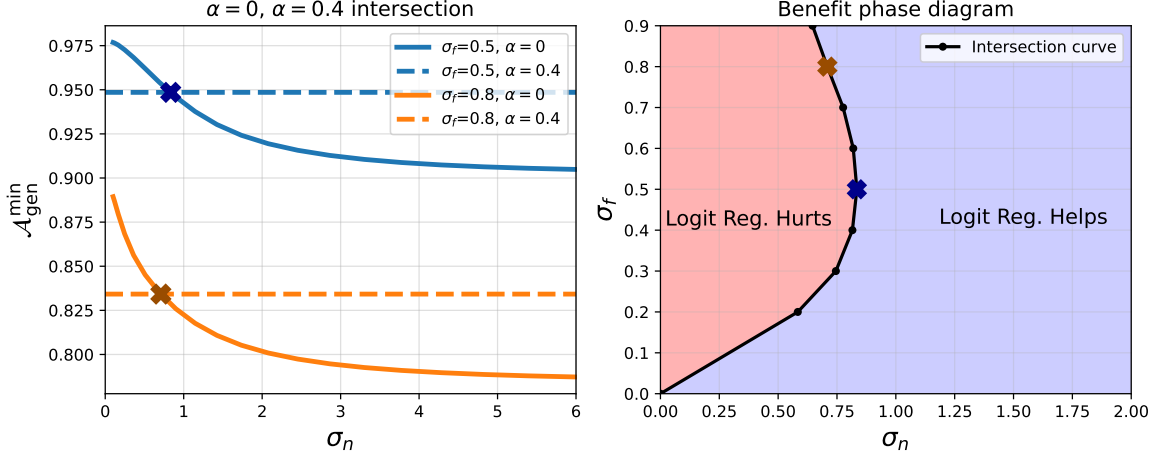


Figure 15. Benefit phase diagram for $\lambda < 1/2$. **Left:** Final generalization accuracy as a function of σ_n , comparing the unregularized ($\alpha = 0$) and regularized ($\alpha > 0$) cases, and for $\lambda = 0.4$. **Right:** Phase diagram showing regions where logit regularization is beneficial. The boundary curve is constructed from the intersection points (as shown in the left panel) for different values of σ_f . For illustration, the intersection points of the unregularized and regularized curves for $\sigma_f = 0.5, 0.8$ (left) are marked as “X”’s of corresponding colors on the boundary curve (right).

E.3. Comprehensive Parameter Sweeps

In this subsection, we present a systematic numerical analysis of the generalization accuracy and the cosine similarity (relative to the true feature axis). We perform parameter sweeps over the aspect ratio λ , signal noise σ_f , and orthogonal noise σ_n , comparing the unregularized baseline ($\alpha = 0$) against the logit-regularized model ($\alpha > 0$).

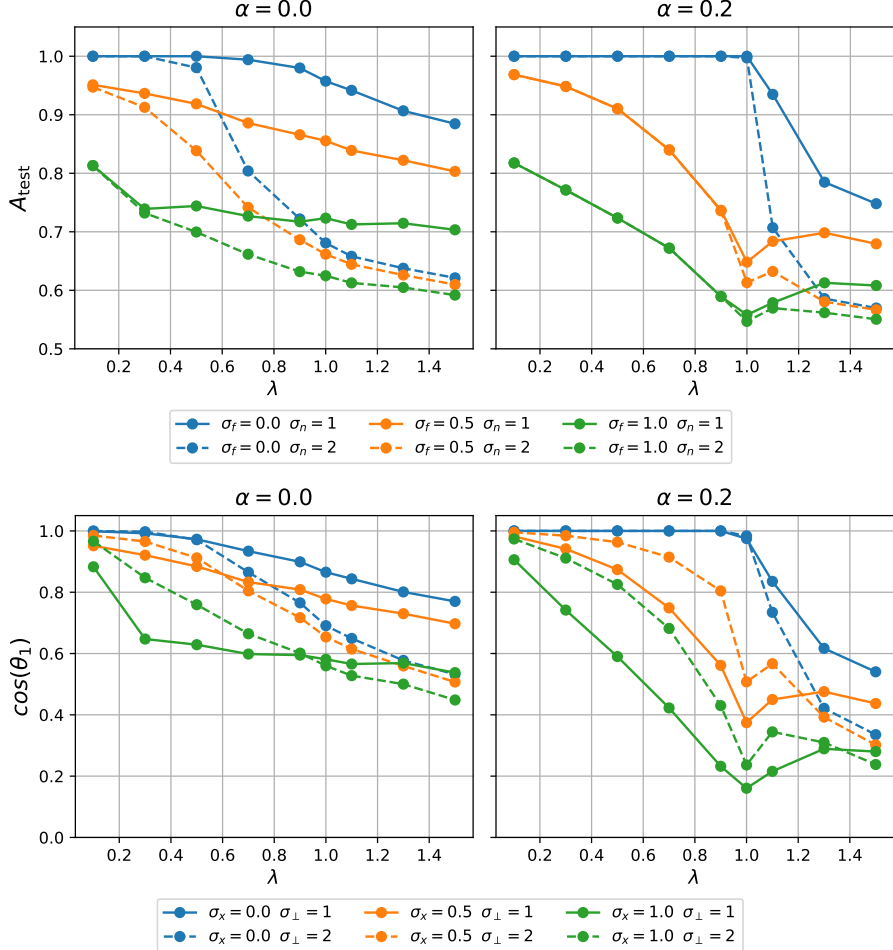


Figure 16. Performance as a function of model capacity ($\lambda = d/N$). **Top Panels:** Generalization accuracy for the unregularized (left) and regularized (right) models. Different colors correspond to signal noise levels $\sigma_f = \{0, 0.5, 1\}$, and solid/dashed lines indicate orthogonal noise levels $\sigma_n = \{1, 2\}$. Two key phenomena are visible in the regularized case (right): (1) The accuracy becomes independent of σ_n for $\lambda < 1$, and (2) For the noiseless feature case ($\sigma_f = 0$), the interpolation threshold shifts from $\lambda = 0.5$ to $\lambda = 1$. **Bottom Panels:** Cosine similarity with the true feature axis. Unlike the accuracy, the cosine similarity remains sensitive to σ_n in both regimes, confirming that regularization stabilizes the prediction quality even while the weight direction varies.

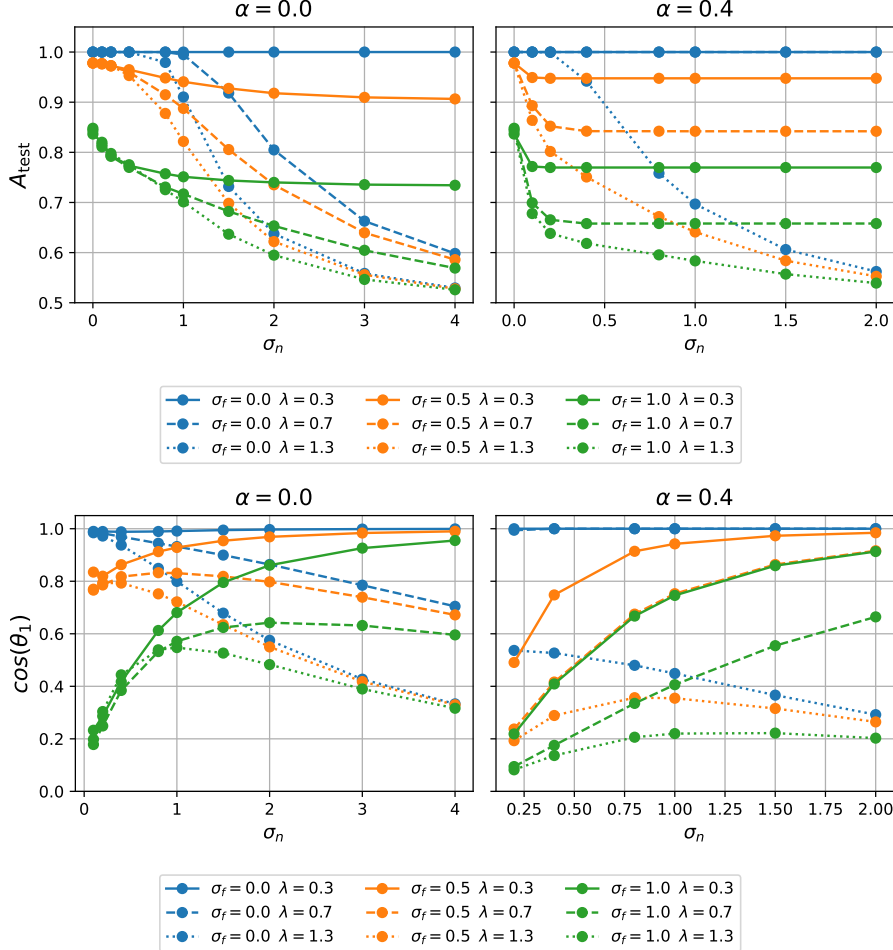


Figure 17. Sensitivity to orthogonal noise amplitude σ_n . **Top Panels:** Generalization accuracy vs. σ_n . The regularized model (right) is robust to changes in σ_n , maintaining constant accuracy. Note: The slight deviation observed at extremely small σ_n is a numerical artifact; the convergence time scales inversely with noise, preventing the simulation from fully reaching the theoretical optimum within the fixed computational budget in the limit $\sigma_n \rightarrow 0$. **Bottom Panels:** Cosine similarity vs. σ_n . Here we observe distinct regimes: for the underparameterized case ($\lambda < 1/2$), increasing noise improves alignment (similarity $\rightarrow 1$), whereas for the overparameterized case ($\lambda > 1/2$), increasing noise degrades alignment.

E.4. Comparison with Weight Decay

To underscore the unique geometric properties of logit regularization, we contrast its effects with standard L_2 parameter regularization (Weight Decay). We consider the objective function:

$$\mathcal{L}_{\text{WD}} = \sum_i \log \left(1 + e^{-y_i \mathbf{S}^\top \mathbf{x}_i} \right) + \frac{\gamma}{2} \|\mathbf{S}\|^2. \quad (33)$$

While Weight Decay prevents the weights from diverging, it fundamentally differs from logit regularization in how it shapes the optimization landscape. As shown in Figure 18, Weight Decay does **not** induce the specific invariance properties observed under logit regularization.

Specifically, we highlight two key distinctions:

1. **No shift in interpolation threshold:** Unlike logit regularization, adding Weight Decay does not shift the interpolation threshold in the noiseless feature regime ($\sigma_f = 0$). The generalization accuracy does not reach 100% throughout the region $\lambda < 1$, confirming that the perfect generalization mechanism (logit clustering around a finite target) is specific to the per-sample convexity of logit penalties.

2. **Sensitivity to orthogonal noise:** The final accuracy under Weight Decay remains explicitly dependent on the orthogonal noise scale σ_n . This stands in sharp contrast to the logit-regularized case, where the accuracy becomes invariant to σ_n (as shown in Figure 16).

It is worth noting that for linear models, quadratic logit regularization (αz^2) can be viewed as a generalized Tikhonov regularization of the form $\alpha \mathbf{S}^\top \hat{\Sigma} \mathbf{S}$, where $\hat{\Sigma} = \frac{1}{N} \sum_i \mathbf{x}_i \mathbf{x}_i^\top$ is the empirical non-centered covariance matrix. This data-dependent structure naturally adapts the penalty to the geometry of the input features, a property that isotropic Weight Decay ($\gamma \mathbf{S}^\top \mathbf{I} \mathbf{S}$) lacks.

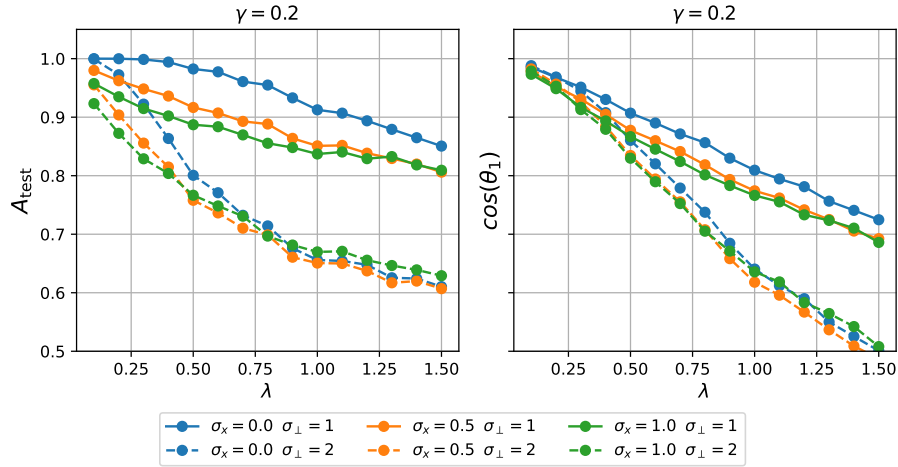


Figure 18. Generalization under Weight Decay. The generalization accuracy (top) and cosine similarity (bottom) achieved at convergence with standard L_2 regularization ($\gamma = 0.2$). Unlike logit regularization, the accuracy remains sensitive to σ_n and does not exhibit perfect generalization in the $\sigma_f = 0$ regime for $0.5 < \lambda < 1$.

E.5. Dependence of Cosine Similarity on Noise Amplitudes

In this subsection, we numerically investigate the alignment of the learned weights with the true signal direction. We measure this via the cosine similarity $\rho = \cos(\theta_1)$, analyzing its dependence on the orthogonal noise σ_n and the signal noise σ_f .

First, we examine the dependence on σ_n . Recall from the main text (Eq. 4) that the alignment is predicted to follow the scaling form:

$$\cos(\theta_1) = \frac{1}{\sqrt{1 + (C/\sigma_n)^2}}, \quad (34)$$

where C is a coefficient that depends on σ_f but is strictly independent of σ_n . This implies a linear relationship between $1/\cos^2(\theta_1)$ and $1/\sigma_n^2$. In Figure 19, we verify this prediction numerically: the data perfectly fits the line $y = 1 + C^2 x$, confirming the validity of our analytical derivation.

Next, we characterize the coefficient C by analyzing its dependence on the signal noise σ_f . We fix $\sigma_n = 1$ and track the components of the weight vector $\mathbf{S} = S_1 \mathbf{e}_1 + \mathbf{S}_{\perp}$. As shown in the left panel of Figure 20, for small σ_f , the signal component S_1 remains approximately constant, while the orthogonal component $\|\mathbf{S}_{\perp}\|$ grows linearly with σ_f . Consequently, the ratio $C \propto \|\mathbf{S}_{\perp}\|/S_1$ exhibits a linear dependence on σ_f in the low-noise regime (see Figure 20, right panel). This demonstrates that as the feature noise vanishes ($\sigma_f \rightarrow 0$), the model relies less on spurious orthogonal correlations, recovering the perfect alignment predicted in the noiseless limit.

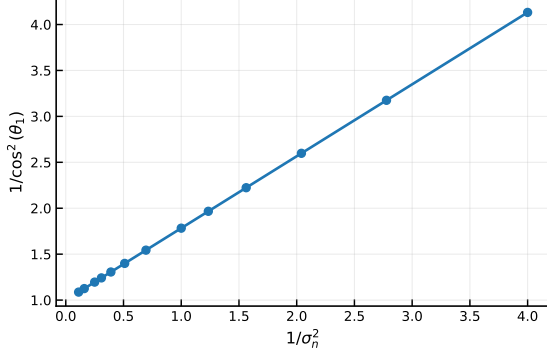


Figure 19. **Verification of σ_n scaling.** Plot of $1/\cos^2(\theta_1)$ versus $1/\sigma_n^2$. The linear fit confirms the functional form derived in Eq. (34), where the slope corresponds to C^2 .

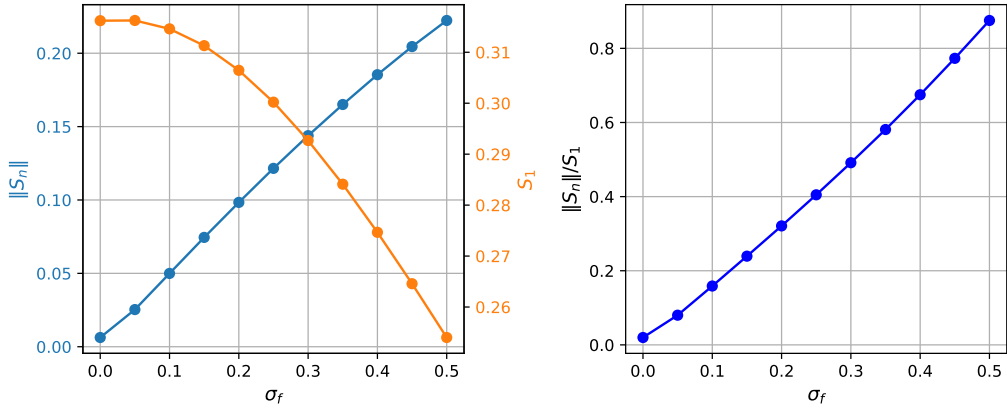


Figure 20. **Dependence on σ_f .** All results are for fixed $\sigma_n = 1$. **Left:** The magnitudes of the orthogonal weight component $\|S_{\perp}\|$ and the signal component S_1 as functions of σ_f . **Right:** The ratio $\|S_{\perp}\|/S_1$ (which is proportional to C) scales linearly with σ_f for small noise amplitudes.

E.6. Additional details regarding the numerical settings

Unless stated otherwise, we consider a linear classification model trained by minimizing the regularized loss $\mathcal{L} = \sum_i [(1 - \alpha)\ell_{\text{CE}}(z_i, y_i) + \alpha z_i^2]$. We use Full-Batch Gradient Descent (GD) for the optimization. The data is generated according to the signal-plus-noise decomposition $\mathbf{x} = y\mu_f \mathbf{e}_1 + \boldsymbol{\xi}$, where $\boldsymbol{\xi} = \sigma_f \boldsymbol{\xi}_f \mathbf{e}_1 + \sigma_n \boldsymbol{\xi}_{\perp}$. In most experiments, the noise components $\boldsymbol{\xi}_f$ and $\boldsymbol{\xi}_{\perp}$ are drawn from standard Normal distributions.

Below we provide the exact hyperparameters used for each figure:

- **Figure 1 (Clustering):**

- **Top Row ($\alpha = 0$):** $d = 1400$, $N = 2000$ ($\lambda = 0.7$), $\mu_f = 1$, $\sigma_f = 0.5$, $\sigma_n = 1$. The model is trained for 20,000 epochs with learning rate $\eta = 0.1$.
- **Bottom Row ($\alpha > 0$):** Same parameters as above, but with $\alpha = 0.2$.
- **Figure 1 (Zero Feature Noise):** Same parameters as above, but with $\sigma_f = 0$ and $\alpha = 0.2$.

- **Figure 2 (Invariance with Student-t Noise):** The noise follows a Student-t distribution with degrees of freedom $\nu \in \{2.1, 3, 20\}$. The dimensions are $d = 1000$, $N = 1500$ ($\lambda \approx 0.67$) with $\mu_f = 1$, $\sigma_f = 1$, $\sigma_n = 1$. For $\alpha = 0$, we use GD with $\eta = 0.1$. For $\alpha > 0$, we use the Adam optimizer with $\eta = 0.001$. The number of epochs varies between 2,000 and 10,000 depending on convergence.

- **Figure 13 (Appendix - Invariance with Gaussian Noise):** Gaussian data with varying dimension $d \in \{200, 1400, 1800\}$ while keeping $N = 2000$ fixed, yielding $\lambda \in \{0.1, 0.7, 0.9\}$. Other parameters: $\mu_f = 1$, $\sigma_f = 0.5$, $\sigma_n = 1$. Trained for 20,000 epochs with GD ($\eta = 0.1$).
- **Figure 16 (Performance vs λ):** We vary d while keeping $N = 2000$ fixed to sweep λ .
 - Parameters: $\mu_f = 1$. Signal noise $\sigma_f \in \{0, 0.5, 1\}$. Orthogonal noise $\sigma_n \in \{0.2, 4\}$.
 - Regularization: We compare $\alpha = 0$ vs $\alpha = 0.4$.
 - Optimization: GD with $\eta = 0.1$ for 20,000 epochs.
- **Figure 18 (WD Performance):** We vary d while keeping $N = 2000$ fixed to sweep λ ,
 - Parameters: $\mu_f = 1$. $\sigma_f \in \{0, 0.5, 1\}$. $\sigma_n \in \{1, 2\}$.
 - Regularization: $\alpha = 0$ but $\gamma = 0.2$ (WD).
 - Optimization: GD with $\eta = 0.1$ for 2,000 epochs.
- **Figure 19 (Cosine Similarity vs σ_n):** We fix $d = 1400$, $N = 2000$ ($\lambda = 0.7$).
 - Parameters: $\mu_f = 1$, $\sigma_f = 0.5$. We sweep $\sigma_n \in [0.5, 3]$.
 - Regularization: $\alpha = 0.2$.
 - Optimization: GD with $\eta = 0.1$ for 2,000 epochs.
- **Figure 20 (Cosine Similarity vs σ_f):** We fix $d = 1400$, $N = 2000$ ($\lambda = 0.7$).
 - Parameters: $\mu_f = 1$, $\sigma_n = 1$. We sweep $\sigma_f \in [0, 0.5]$.
 - Regularization: $\alpha = 0.4$.
 - Optimization: Adam optimizer with $\eta = 0.01$ for 1,000 epochs.
- **Figure 5 (Grokking):** We fix $d = 1400$, $N = 2000$ ($\lambda = 0.7$) in the noiseless feature regime.
 - Parameters: $\mu_f = 0.1$, $\sigma_f = 0$, $\sigma_n = 1$.
 - Regularization: We compare $\alpha \in \{0, 0.001, 0.01, 0.1\}$.
 - Optimization: GD with $\eta = 0.1$ for an extended duration of 200,000 epochs.
- **Figure 6 (Phase Diagram $\lambda = 0.7$):** $d = 1400$, $N = 2000$. We interpolate theoretical curves based on simulations with σ_n sweeping from 0.1 to 6.
 - Parameters: $\mu_f = 1$, $\alpha = 0.4$.
 - Optimization: GD with $\eta = 0.1$ for 20,000 epochs.
- **Figure 15 (Phase Diagram $\lambda = 0.4$):** $d = 800$, $N = 2000$.
 - Parameters: $\mu_f = 1$, $\alpha = 0.4$.
 - Optimization: GD with $\eta = 0.1$ for 20,000 epochs.
- **Figure 7 (Multi-class):** $K = 10$ classes. $d = 1400$, $N = 2000$ ($\lambda = 0.7$).
 - Parameters: $\mu_f = 1$, $\sigma_f = 0.1$, $\sigma_n = 1$.
 - Regularization: $\alpha = 0$ and $\alpha = 0.2$.
 - Optimization: GD optimizer with $\eta = 0.1$ for 20,000 epochs.
- **Figure 8 (Multi-class Grokking):** $K = 10$ classes. $d = 1400$, $N = 2000$ ($\lambda = 0.7$). Same as previous but for $\sigma_f = 0$ and $\alpha = 0.04$.

E.6.1. RESNET-18 (FIGURES 3 AND 9)

We extract 512-dimensional penultimate features from a frozen ResNet-18 pre-trained on ImageNet. For the linear probe experiments, we select $N_{\text{train}} = 1000$ balanced training samples and use the remaining $N_{\text{test}} = 9000$ samples for evaluation. We compare performance on the clean CIFAR-10 test set and on CIFAR-10-C (Impulse Noise, Severity 5).

Feature Decomposition and Noise Estimation: To map the complex feature distribution to our theoretical signal-plus-noise model, we perform a class-conditional decomposition. Let $X \in \mathbb{R}^{N \times d}$ be the matrix of feature vectors and y the labels. For each class c , we compute the empirical mean $\mu_c \in \mathbb{R}^d$ and the centered covariance matrix Σ_c .

1. **Signal Subspace:** We define the signal subspace \mathcal{S} as the span of the differences between class means, $\mathcal{S} = \text{span}(\{\mu_c - \mu_1\}_{c=2}^K)$. We compute an orthonormal basis $Q_1 \in \mathbb{R}^{d \times (K-1)}$ for \mathcal{S} via QR decomposition.
2. **Orthogonal Subspace:** We complete the basis to \mathbb{R}^d using an orthogonal complement $Q_2 \in \mathbb{R}^{d \times (d-K+1)}$, such that $U = [Q_1, Q_2]$ is unitary.
3. **Noise Projection and RMS Calculation:** We project the class-conditional covariances onto these subspaces. The effective noise amplitudes reported in the figures are calculated as the root-mean-square (RMS) of the standard deviations in each subspace, averaged over all classes:

$$\sigma_f^{\text{eff}} = \frac{1}{K} \sum_{c=1}^K \sqrt{\text{Tr}(Q_1^\top \Sigma_c Q_1) / \dim(\mathcal{S})}, \quad \sigma_n^{\text{eff}} = \frac{1}{K} \sum_{c=1}^K \sqrt{\text{Tr}(Q_2^\top \Sigma_c Q_2) / \dim(\mathcal{S}^\perp)}. \quad (35)$$

To allow for comparison across datasets with different signal scales, we normalize these values by the mean pairwise distance between class centroids.

Synthetic Orthogonal Scaling: To verify the invariance to orthogonal noise (Fig. 11, Right), we synthetically manipulate the data geometry. We project every feature vector \mathbf{x}_i onto the orthogonal subspace via the projection matrix $P_\perp = Q_2 Q_2^\top$ and scale this component by a factor γ :

$$\mathbf{x}_i^{\text{scaled}} = (I - P_\perp) \mathbf{x}_i + \gamma P_\perp \mathbf{x}_i. \quad (36)$$

This operation scales the effective σ_n by γ while preserving the signal geometry exactly. The linear classifier is then trained on these scaled features using the Adam optimizer ($\eta = 10^{-4}$) for 30,000 epochs.